

Simulation of high-Mach-number inviscid flows using a third-order Runge-Kutta and fifth-order WENO-based finite-difference lattice Boltzmann method

Akshay U. Shirsat , Sagar G. Nayak , and Dhiraj V. Patil **Department of Mechanical, Materials, and Aerospace Engineering, Indian Institute of Technology Dharwad, Dharwad, Karnataka 580011, India*

(Received 27 June 2022; accepted 1 August 2022; published 23 August 2022)

A discrete-velocity Boltzmann equation (DVBE) with Bhatnagar-Gross-Krook (BGK) approximation is discretized in time and space using a third-order Runge-Kutta (RK3) and fifth-order weighted essentially nonoscillatory (WENO) finite-difference scheme to simulate benchmark inviscid compressible flows. The implementation of the WENO ensures that solutions behave with minimal or no oscillations, narrowing the gap between the exact and the numerical results. Discrete-velocity sets given by Kataoka and Tsutahara [*Phys. Rev. E* **69**, 056702 (2004)] are used. The additional dissipation terms as well as artificial viscosity are incorporated in the formulation to solve the compressible flows at high Mach number. Further, the flows which are subjected initially to a high density ratio are effectively simulated. In this article, one-dimensional benchmarks are simulated at initial Mach number up to 30 and density ratio up to 1000, whereas, the benchmarks in two dimensions are simulated with a Mach number up to 10. The algorithm is assessed by simulating numerous benchmarks, namely, (i) one-dimensional Riemann problem for various shock waves combinations [namely (a) shock-shock waves in the case of different Mach numbers, (b) rarefaction-shock waves for various density ratios, (c) sudden contact shock discontinuity, and (d) shock-rarefaction waves for density ratio 5], (ii) isentropic vortex convection test, (iii) regular shock reflection (RR) for Mach numbers 2.9 and 10, (iv) double Mach reflection (DMR) for inflow Mach numbers as 6 and 10, and (v) forward-facing step for inflow Mach numbers 2 to 5. Further, the effect of change in Mach numbers and wedge angles on the flow structures in the case of DMR are detailed. In the case of a forward-facing step, the variations of flow structure (e.g., the Mach stem height, triple points location, and shock standoff distance) are detailed with respect to Mach number, step height, and specific-heat ratios. Finally, the numerical stability of the proposed formulation is carried out to assess the behavior of the free parameters.

DOI: [10.1103/PhysRevE.106.025314](https://doi.org/10.1103/PhysRevE.106.025314)

I. INTRODUCTION

The lattice Boltzmann equation (LBE) method has matured in the past three decades and is now one of the popular tools for solving various fluid flow problems. In the LBE method, the particle distributions are evolved on a regular lattice structure. The discrete-velocity Boltzmann equation (DVBE) is solved with a chosen velocity set at a discrete-spatial node satisfying the conservation laws, Galilean invariance, etc. In LBE, due to the coupled velocity and spatial discretization, the streaming process is straightforward with only a near-neighbor shift and hence exhibits high parallel computing efficiency. The lattice Boltzmann equation is subjected to the Chapman-Enskog expansion analysis to recover the macroscopic equations [1–3]. The LBE method is used for simulation of a variety of fluid flow problems such as incompressible flows, multiphase flows, high-Knudsen-number flows, flow through porous medium and microchannels, turbulent flows, and many more.

The coupled space-velocity discretization limits the application of LBE method on the uniform square and cubic Cartesian meshes. However, recent developments allow use of rectangular meshes [4–6]. The coupling restricts the choice

of discrete velocities, as “off-lattice” velocity sets need interpolation or extrapolation while streaming the distribution functions. However, in the case of compressible flows, microflows, and multicomponent flows, it is desirable to use general discrete velocities that may not be suited to lattice structures [7]. Few efforts have been made to broaden the applications of a standard LBE method to nonregular (i.e., nonuniform, unstructured) meshes, and several so-called the off-lattice Boltzmann (OLB) methods have been developed using various schemes such as finite difference [8,9], finite volume [10,11], and finite element [12–14]. These OLB methods vary from each other in the temporal and spatial discretizations, for example, OLB methods are constructed, by using a time-splitting strategy in solving the DVBE [14,15] where it is decomposed into a collision subequation and followed by a pure advection subequation. The collision is entirely local and discretized directly which is similar to the traditional LBE whereas the advection of the distribution is handled using various schemes, e.g., flux balance.

In the case of high-Mach-number (Ma) simulation, the compressibility effects are more pronounced [16]. Such high-speed flows are employed to understand the flow over aircraft, aerodynamics, flow through jet engines, gas pipelines, rocket motors, re-entry flows, and many others. A robust high-Mach-number LB solver may be employed for such problems. LBE method has been successful in simulating the incompressible

*dhiraj@iitdh.ac.in

flows and weakly compressible flows, but it has encountered difficulties while simulating high-Mach-number compressible fluid flow problems. This error is attributed to the low-Mach-number assumption in the truncated Taylor series expansion while deriving the equilibrium distribution function in the traditional LBE method and the restrictions on the lattice velocity sets. Various attempts to simulate compressible fluid flows are summarized as follows: Alexander *et al.* [17] proposed a model which allowed selecting speed of sound by carefully selecting parameters from the equilibrium distribution function. They suggested lowering the speed of sound to increase the Mach number; however, the model only works for nearly isothermal compressible systems. Qian [18] derived a nonlinear deviation term using Chapman-Enskog expansion and numerically simulated one-dimensional shock-tube problem. Sun [19] proposed an adaptive model where the particle microscopic velocity was accounted by using local fluid velocity and internal energy. The model was able to simulate the flow up to 2.9 Mach. The same model was extended further which was able to simulate problems up to Mach 10 [20]. Yu and Zhao [21] proposed an alternative to the model given by Alexander *et al.* [17] by introducing an attractive forcing term. This addition helped in an effective softening of the sound speed hence enabling the model to simulate high Mach numbers. The model was able to reproduce the flow up to 5.09 Mach.

Further, Kataoka and Tsutahara [22] in 2004 proposed finite-difference lattice Boltzmann (FD-LB) scheme for compressible Euler flows. The scheme overcomes the earlier limitation on the restriction of the specific heat ratio. Furthermore, the scheme uses the D2Q9 model instead of the D2Q17 model [23], which helps to reduce the computational time. However, numerical instabilities are seen for flows with Mach numbers more than unity. The stability issue associated with the LBE method at a high Mach number is addressed profusely in the literature. Many efforts have been made to eliminate or at least reduce the instabilities from the compressible flows LB models to widen the applicability [24]. Popular techniques to improve numerical stability include the flux limiter method [8], multiple-relaxation time for compressible flows [25], and addition of dispersion and artificial viscosity [26,27]. Over the years, Kataoka and others have proposed different compressible LB models as well [28–30]. Watari [31] proposed FD-LB models for the viscous and inviscid flows in two dimensions (2D) and three dimensions (3D), respectively. In his work, the 3D Euler model consisted of 12 microscopic velocities, which was an improvement compared to the D3Q15 model of Kataoka and Tsutahara [22]. Yan *et al.* [32] proposed a three-speed and energy level D2Q25 model and were able to simulate the flow up to 4.0 Mach. Next, Gan *et al.* [27] proposed an improved model based on the thermal model by Watari and Tsutahara [33], which eliminated the constraint of selecting equal relaxation time and time step. Attempts have been made to couple the double-distribution function (DDF) approach with the multispeed models to simulate the compressible fluid flows [34–36]. Recently, several other methods such as density- and pressure-based regularized LBM (referred to as HRR- ρ and HRR-p, respectively) [37,38], hybrid lattice Boltzmann method (HLBM) [39–41], and semi-Lagrangian lattice Boltzmann method (SLLBM)

[42–45] have been proposed to simulate compressible flows.

The presence of shock and contact discontinuities in high-speed compressible flows necessitates design of numerical schemes which can capture these features while avoiding spurious oscillations. The commonly used CFD methods to generate nonoscillatory solutions are ENO and WENO [46]. The WENO scheme concept was originally utilized by Liu *et al.* [47] and enhanced further by Jiang and Shu [48], and uses weighted stencils for the ENO scheme. Unlike ENO, WENO scheme considers all the possible stencils instead of picking only the smooth one. Hence, it has improved the accuracy and resolution [49]. Further, various other aspects of WENO scheme such as FV and FD implementations, time integration, and order of convergence are discussed in detail by Shu [50]. The WENO-based study on different lattice Boltzmann flux solvers (LBFS) has been carried out in the past. In the LBFS, the local solution of 1D- and 2D-LB model is used to construct the flux solver at the cell interface. The LBFS can provide good positivity property for simulation of flows with shock waves and can be well applied to simulate both compressible and incompressible flows. Further, it gives greater flexibility in the case of nonuniform meshes and complex geometries. Also, the memory storage for the simulation result decreased substantially and the boundary conditions can be implemented easily. The performance and systematic investigation pertaining to its accuracy, stability, and efficiency needs to be carried out [51]. Finite-difference WENO (FD-WENO) [48,52–54] and finite-volume WENO (FV-WENO) [55,56] are implemented by incorporating the Runge-Kutta (RK) scheme for time discretization and fifth-order compact FD scheme for space discretization have been considered in the literature. Shu has suggested [49] use of FD-WENO scheme in practice, due to the high accuracy, high resolution, and minimal set of calculations. In this work, third-order RK in time and fifth-order WENO scheme in space are implemented to minimize the numerical oscillations and to achieve high order accuracy for FD-LB algorithm proposed by Kataoka and Tsutahara [22] with additional terms as suggested by Pan *et al.* [26]. This coupling is done to ensure that the resulting scheme is TVD. The proposed RK3 + WENO finite-difference approach to solve DVBE instead of the traditional collision-streaming methodology may add computational overheads leading to deterioration in the compute performance.

The classical 1D Riemann problem is crucial to benchmark as it exhibits abrupt changes in the properties across the two adjacent domains [57]. Hence, RK3 + WENO-based FD-LB algorithm is first assessed for three 1D benchmark problems, namely, 1D Riemann problem, shock-tube problem, and contact discontinuity. Further, the shock reflection and associated flow structures due to the presence of wedge in the flow form an interesting benchmark for the oblique shock solution [58,59]. The 2D double Mach reflection (DMR) and the supersonic inviscid flow over forward-facing step are extensively used for assessing numerical schemes [60–62]. In this article, the applicability of the algorithm is demonstrated by simulating these 2D problems. Further, the effect of Mach number and wedge angle is studied in case of 2D-DMR. The variations in the flow structures are obtained by varying the

inlet Mach number, step height, and specific heat ratio for the flow over the forward-facing step.

The rest of the paper is organized as follows. Section II presents the FD-LB methodology with RK3 and fifth-order WENO for one- and two-dimensional computational domains. Section III presents numerical simulations for assessing the RK3 + WENO-based FD-LB method. The algorithm is assessed by simulating numerous benchmarks, namely, (i) 1D Riemann problem for various combinations of wave [(a) shock-shock waves for different Mach numbers, (b) rarefaction-shock waves for different density ratios, (c) sudden contact shock discontinuity, and (d) shock-rarefaction waves], (ii) isentropic vortex convection test, (iii) regular shock reflection (RR) for Mach numbers 2.9 and 10, (iv) DMR for inflow Mach numbers as 6 and 10, and (v) forward-facing step for inflow Mach numbers 2 to 5, step height, and specific heat ratio variation. Finally, Sec. IV draws conclusions and perspectives on the work.

II. MATHEMATICAL FORMULATION

The lattice Boltzmann equation can be derived from the full Boltzmann equation [63,64]. The Boltzmann equation with the Bhatnagar-Gross-Krook (BGK) approximation is written as [1]

$$\frac{\partial f_i}{\partial t} + c_{i\beta} \frac{\partial f_i}{\partial x_\beta} = \frac{1}{\tau} (f_i^{\text{eq}} - f_i), \quad (1)$$

with the initial conditions

$$f_i = f_i^{\text{eq}}(\rho^0, u_\beta^0, T^0), \quad (2)$$

where f_i^{eq} is the discrete local equilibrium distribution function, superscript 0 represents the initial physical values, and $c_{i\beta}$ is the discrete particle velocity, $i = 0, 1, 2, \dots, N-1$, where N is the total number of discrete velocity components, τ is the BGK relaxation time, and β and γ represent spatial coordinates. Further, η_i is introduced to govern the specific heat ratio. The above equation is a typical workhorse of the LBE method and approximates the Navier-Stokes equations in the CFD with continuum approximation in certain situations such as when higher order contributions $O(\text{Kn}^2)$ and $O(\text{Ma}^4)$ tends to zero [65]. The nondimensional variables and equations, which are convenient for the numerical analysis and calculation, are listed below. Let L , ρ_0 , and T_0 represent the reference length, density, and temperature, respectively, and the nondimensional variables are defined in Ref. [22] as $\hat{t} = \frac{t}{L/\sqrt{RT_0}}$, $\hat{x}_\beta = \frac{x_\beta}{L}$, $\hat{c}_{i\beta} = \frac{c_{i\beta}}{\sqrt{RT_0}}$, $\hat{\eta}_i = \frac{\eta_i}{\sqrt{RT_0}}$, $\hat{f}_i = \frac{f_i}{\rho_0}$, $\hat{f}_i^{\text{eq}} = \frac{f_i^{\text{eq}}}{\rho_0}$, $\hat{\rho} = \frac{\rho}{\rho_0}$, $\hat{u}_\beta = \frac{u_\beta}{\sqrt{RT_0}}$, $\hat{T} = \frac{T}{T_0}$, and $\hat{p} = \frac{p}{\rho_0 RT_0}$. The nondimensional flow variables which are derived in the LBE method using the moments of the discrete distribution functions are defined as

$$\hat{\rho} = \sum_{i=0}^{N-1} \hat{f}_i, \quad (3)$$

$$\hat{\rho} \hat{u}_\beta = \sum_{i=0}^{N-1} \hat{f}_i \hat{c}_{i\beta}, \quad (4)$$

$$\hat{\rho} (b\hat{T} + \hat{u}_\beta^2) = \sum_{i=0}^{N-1} \hat{f}_i (\hat{c}_{i\beta}^2 + \hat{\eta}_i^2). \quad (5)$$

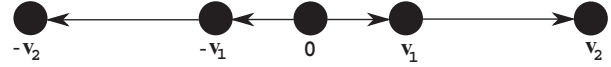


FIG. 1. D1Q5 lattice model.

Hence, the kinetic Eq. (1) in the nondimensional form is

$$\frac{\partial \hat{f}_i}{\partial \hat{t}} + \hat{c}_{i\beta} \frac{\partial \hat{f}_i}{\partial \hat{x}_\beta} = \frac{1}{\epsilon} (\hat{f}_i^{\text{eq}} - \hat{f}_i), \quad (6)$$

where ϵ is the Knudsen number defined by

$$\epsilon = \frac{\tau \sqrt{RT_0}}{L}. \quad (7)$$

Here, \hat{f}_i^{eq} satisfies the following constraints,

$$\hat{\rho} = \sum_{i=0}^{N-1} \hat{f}_i^{\text{eq}}, \quad (8)$$

$$\hat{\rho} \hat{u}_\beta = \sum_{i=0}^{N-1} \hat{f}_i^{\text{eq}} \hat{c}_{i\beta}, \quad (9)$$

$$\hat{\rho} \hat{\delta}_{\beta\gamma} + \hat{\rho} \hat{u}_\beta \hat{u}_\gamma = \sum_{i=0}^{N-1} \hat{f}_i^{\text{eq}} \hat{c}_{i\beta} \hat{c}_{i\gamma}, \quad (10)$$

$$\hat{\rho} (b\hat{T} + \hat{u}_\beta^2) = \sum_{i=0}^{N-1} \hat{f}_i^{\text{eq}} (\hat{c}_{i\beta}^2 + \hat{\eta}_i^2), \quad (11)$$

$$\hat{\rho} [(b+2)\hat{T} + \hat{u}_\gamma^2] \hat{u}_\beta = \sum_{i=0}^{N-1} \hat{f}_i^{\text{eq}} (\hat{c}_{i\gamma}^2 + \hat{\eta}_i^2) \hat{c}_{i\beta}. \quad (12)$$

The pressure-field \hat{p} is computed from the $\hat{\rho}$ and \hat{T} using the nondimensional equation of state ($\hat{p} = \hat{\rho} \hat{T}$). The common terminologies used in LBE method for referring the dimension of the problem (m) and the number of streaming directions (n) are represented as $DmQn$. It is worth noting that the macroscopic behavior of the Euler equations cannot be fully recovered by Eqs. (8)–(12) as these equilibrium moments relate only to convective fluxes but not diffusive fluxes [22]. The models used for solving one- and two-dimensional compressible flow problems following Ref. [22] are discussed subsequently.

1. One-dimensional lattice structure ($m = 1, n = 5$)

The D1Q5 lattice structure (as shown in Fig. 1) discrete velocities are given as

$$\hat{c}_{i1} = \begin{cases} (0) & i = 0; \\ v_1 \cos(i+1)\pi & i = 1, 2; \\ v_2 \cos(i+1)\pi & i = 3, 4. \end{cases} \quad (13)$$

The $\hat{\eta}_i$ in Eq. (12) for each discrete velocity component is given as

$$\hat{\eta}_i = \begin{cases} \eta_0 & i = 0; \\ 0 & i = 1, 2, 3, 4. \end{cases} \quad (14)$$

In Eqs. (13) and (14), $v_1, v_2 (\neq v_1)$ and η_0 are given nonzero constants. v_1 is generally taken as inlet Mach number, v_2 is two times v_1 , and η_0 is average of v_1 and v_2 , as per numerical problem setup. Further, the Courant-Friedrichs-Lewy (CFL) number can be calculated using Δt and Δx as

CFL = $v_2 \Delta t / \Delta x$. The local equilibrium distribution function in the nondimensional form given in Eq. (6) is obtained as [22]

$$\hat{f}_i^{\text{eq}} = \hat{\rho}(A_i + B_i \hat{u}_1 \hat{c}_{i1}), \quad (15)$$

where

$$A_i = \begin{cases} \frac{b-1}{\eta_0} \hat{T} & i = 0; \\ \frac{1}{2(v_1^2 - v_2^2)} \left[-v_2^2 + \left((b-1) \frac{v_2^2}{\eta_0} + 1 \right) \hat{T} + \hat{u}_1^2 \right] & i = 1, 2; \\ \frac{1}{2(v_2^2 - v_1^2)} \left[-v_1^2 + \left((b-1) \frac{v_1^2}{\eta_0} + 1 \right) \hat{T} + \hat{u}_1^2 \right] & i = 3, 4. \end{cases} \quad (16)$$

$$B_i = \begin{cases} \frac{-v_2^2 + (b+2)\hat{T} + \hat{u}_1^2}{2v_1^2(v_1^2 - v_2^2)} & i = 1, 2; \\ \frac{-v_1^2 + (b+2)\hat{T} + \hat{u}_1^2}{2v_2^2(v_2^2 - v_1^2)} & i = 3, 4. \end{cases} \quad (17)$$

Here, $b = \frac{2}{(\gamma-1)}$ is a given constant, where γ is the specific heat ratio and \hat{c}_{i1} , $\hat{\eta}_i$, \hat{f}_i^{eq} given above satisfies the constraints given by Eqs. (8)–(12).

2. Two-dimensional model ($m = 2, n = 9$)

The D2Q9 lattice structure (as shown in Fig. 2) discrete velocities are given as

$$(\hat{c}_{i1}, \hat{c}_{i2}) = \begin{cases} (0, 0) & i = 0; \\ v_1 \left[\cos \frac{(i+1)\pi}{2}, \sin \frac{(i+1)\pi}{2} \right] & i = 1, 2, 3, 4; \\ v_2 \left[\cos \pi \left(\frac{(i+1)}{2} + \frac{1}{4} \right), \sin \pi \left(\frac{(i+1)}{2} + \frac{1}{4} \right) \right] & i = 5, 6, 7, 8; \end{cases} \quad (18)$$

and

$$\hat{\eta}_i = \begin{cases} \eta_0 & i = 0; \\ 0 & i = 1, 2, 3, \dots, 8. \end{cases} \quad (19)$$

In Eqs. (18) and (19), v_1 , v_2 ($\neq v_1$), and η_0 are given nonzero constants as described subsequently:

$$f_i^{\text{eq}} = \hat{\rho}(A_i + B_i \hat{u}_\beta \hat{c}_{i\beta} + D_i \hat{u}_\beta \hat{c}_{i\beta} \hat{u}_\gamma \hat{c}_{i\gamma}), \quad (20)$$

where

$$A_i = \begin{cases} \left(\frac{b-2}{\eta_0} \right) T & i = 0; \\ \frac{1}{4(v_1^2 - v_2^2)} \left[-v_2^2 + \left((b-2) \frac{v_2^2}{\eta_0} + 2 \right) T + \frac{v_2^2}{v_1^2} u_\beta^2 \right] & i = 1, 2, 3, 4; \\ \frac{1}{4(v_2^2 - v_1^2)} \left[-v_1^2 + \left((b-2) \frac{v_1^2}{\eta_0} + 2 \right) T + \frac{v_1^2}{v_2^2} u_\beta^2 \right] & i = 5, 6, 7, 8; \end{cases} \quad (21)$$

$$B_i = \begin{cases} \frac{-v_2^2 + (b+2)T + u_\gamma^2}{2v_1^2(v_1^2 - v_2^2)} & i = 1, 2, 3, 4; \\ \frac{-v_1^2 + (b+2)T + u_\gamma^2}{2v_2^2(v_2^2 - v_1^2)} & i = 5, 6, 7, 8; \end{cases} \quad (22)$$

$$D_i = \begin{cases} \frac{1}{2v_1^4} & i = 1, 2, 3, 4; \\ \frac{1}{2v_2^4} & i = 5, 6, 7, 8; \end{cases} \quad (23)$$

where $\hat{c}_{i\beta}$, $\hat{\eta}_i$, and \hat{f}_i^{eq} given above satisfy the constraints given by Eqs. (8)–(12). From this point onward, the nondimensional notation ($\hat{\cdot}$) is dropped with assumption of the nondimensionality of the equations and boundary conditions. As stated earlier, the salient highlights of finding regarding the values of v_1 , v_2 , and η_0 from different problems imply choosing the value of v_1 to be equal to inlet Mach number. Further, in the case of the rarefaction shock wave problem, the inflow Mach number is zero; however, for the consideration of high-density ratio, a small value of v_1 is considered. It should be noted that the claim of v_1 equal to inlet Mach number is empirical, which if represented mathematically, would become equal to $\sqrt{\gamma T} \text{Ma}$.

A. Space discretization using WENO scheme

A conservative finite-difference spatial discretization for partial derivatives [employed in Eq. (6)] may be obtained [46], e.g., for $\frac{\partial f_i}{\partial x}$ as

$$\frac{\partial f_i}{\partial x} \Big|_{p,q} = \frac{1}{\Delta x} \left(f_i \Big|_{p+\frac{1}{2},q} - f_i \Big|_{p-\frac{1}{2},q} \right), \quad (24)$$

where $f_i|_{p+\frac{1}{2},q}$ is the distribution function calculated at $(p + \frac{1}{2}, q)$, which is a function of several neighboring values of the distribution function $f(x_\beta, t)$. Since the value of $f_i|_{p+\frac{1}{2},q}$ depends upon the stencil, which needs to be chosen depending

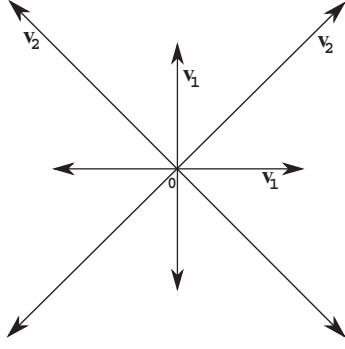


FIG. 2. D2Q9 lattice model.

on $c_{i1} \geq 0$ or $c_{i1} < 0$, two stencils are possible. For achieving fifth-order accuracy in the smooth regions, three stencils containing three grid points in each stencil are considered as shown in Fig. 3.

The stencil shown in Fig. 3(a) represents the stencil for $c_{i1} \geq 0$, where it is left-biased because of the greater number of points on the left side of $f_i|_{p+\frac{1}{2},q}$. On the other hand, the stencil shown in Fig. 3(b) is right-biased and it is used for $c_{i1} < 0$. $f_i^+|_{p+\frac{1}{2},q}$ is utilized for approximating the distribution function biased to the left, whereas $f_i^-|_{p+\frac{1}{2},q}$ is utilized for approximating the distribution function biased to the right. $f_i|_{p+\frac{1}{2},q}$ is calculated as given in Eq. (25),

$$f_i|_{p+\frac{1}{2},q} = f_i^+|_{p+\frac{1}{2},q} + f_i^-|_{p+\frac{1}{2},q}. \quad (25)$$

Calculation of $f_i|_{p+\frac{1}{2},q}$

a. *Case I.* As stated earlier, when the $c_{i1} \geq 0$, the stencil biased to the left is considered. The weights corresponding to each stencil are given by w_k , where $k = 1, 2, 3$ represents stencils comprising lattice nodes:

$$f_i^+|_{p+\frac{1}{2},q} = \sum_{k=1}^3 w_k f_i^k|_{p+\frac{1}{2},q}. \quad (26)$$

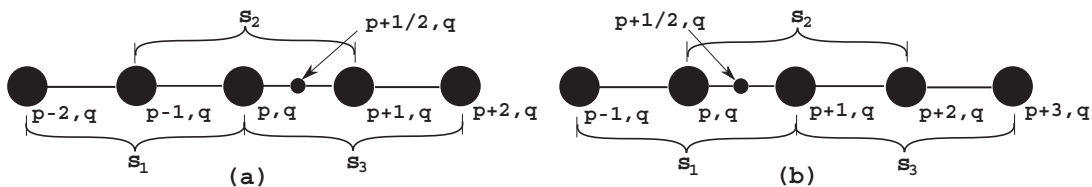
Now, each individual stencil contribution can be written as

$$f_i^1|_{p+\frac{1}{2},q} = \frac{1}{3}f_i|_{p-2,q} - \frac{7}{6}f_i|_{p-1,q} + \frac{11}{6}f_i|_{p,q}, \quad (27)$$

$$f_i^2|_{p+\frac{1}{2},q} = -\frac{1}{6}f_i|_{p-1,q} + \frac{5}{6}f_i|_{p,q} + \frac{1}{3}f_i|_{p+1,q}, \quad (28)$$

and

$$f_i^3|_{p+\frac{1}{2},q} = \frac{1}{3}f_i|_{p,q} + \frac{5}{6}f_i|_{p+1,q} - \frac{1}{6}f_i|_{p+2,q}. \quad (29)$$

FIG. 3. Stencils used for the calculation of $f_i|_{p+\frac{1}{2},q}$: (a) stencil biased to the left and (b) stencil biased to the right.

The weighting factors w_k in Eq. (26) are given by

$$w_k = \frac{\overline{w}_k}{\overline{w}_1 + \overline{w}_2 + \overline{w}_3}, \quad \overline{w}_k = \frac{\delta_k}{(10^{-6} + \sigma_k)^2}, \quad (30)$$

with $\delta_1 = 1/10$, $\delta_2 = 3/5$, and $\delta_3 = 3/10$. The small value 10^{-6} is added to the denominator to avoid dividing by zero. The coefficient σ_k in Eq. (30) are the smoothness indicators and can be obtained following [46] as

$$\sigma_1 = \frac{13}{12}(f_i|_{p-2,q} - 2f_i|_{p-1,q} + f_i|_{p,q})^2 + \frac{1}{4}(f_i|_{p-2,q} - 4f_i|_{p-1,q} + 3f_i|_{p,q})^2, \quad (31)$$

$$\sigma_2 = \frac{13}{12}(f_i|_{p-1,q} - 2f_i|_{p,q} + f_i|_{p+1,q})^2 + \frac{1}{4}(f_i|_{p-1,q} - f_i|_{p+1,q})^2, \quad (32)$$

and

$$\sigma_3 = \frac{13}{12}(f_i|_{p,q} - 2f_i|_{p+1,q} + f_i|_{p+2,q})^2 + \frac{1}{4}(3f_i|_{p,q} - 4f_i|_{p+1,q} + f_i|_{p+2,q})^2. \quad (33)$$

b. *Case II.* As stated earlier, when the $c_{i1} < 0$, the stencil is biased to the right:

$$f_i^-|_{p+\frac{1}{2},q} = \sum_{k=1}^3 w_k f_i^k|_{p+\frac{1}{2},q}. \quad (34)$$

Now, each individual stencil contribution can be written as

$$f_i^1|_{p+\frac{1}{2},q} = -\frac{1}{6}f_i|_{p-1,q} + \frac{5}{6}f_i|_{p,q} + \frac{1}{3}f_i|_{p+1,q}, \quad (35)$$

$$f_i^2|_{p+\frac{1}{2},q} = \frac{1}{3}f_i|_{p,q} + \frac{5}{6}f_i|_{p+1,q} - \frac{1}{6}f_i|_{p+2,q}, \quad (36)$$

and

$$f_i^3|_{p+\frac{1}{2},q} = \frac{11}{6}f_i|_{p+1,q} - \frac{7}{6}f_i|_{p+2,q} + \frac{1}{3}f_i|_{p+3,q}. \quad (37)$$

The weighting factors w_k in Eq. (34) are given by Eq. (30) with $\delta_1 = 3/10$, $\delta_2 = 3/5$, and $\delta_3 = 1/10$. The coefficient σ_k in Eq. (34) are the smoothness indicators and can be obtained by

$$\sigma_1 = \frac{13}{12}(f_i|_{p-1,q} - 2f_i|_{p,q} + f_i|_{p+1,q})^2 + \frac{1}{4}(f_i|_{p-1,q} - 4f_i|_{p,q} + 3f_i|_{p+1,q})^2, \quad (38)$$

$$\sigma_2 = \frac{13}{12}(f_i|_{p,q} - 2f_i|_{p+1,q} + f_i|_{p+2,q})^2 + \frac{1}{4}(f_i|_{p+2,q} - f_i|_{p,q})^2, \quad (39)$$

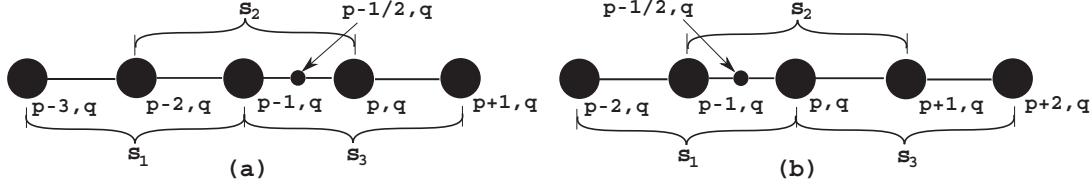


FIG. 4. Stencils used for the calculation of $f_i|_{p-\frac{1}{2},q}$: (a) stencil biased to the left and (b) stencil biased to the right.

and

$$\sigma_3 = \frac{13}{12} (f_i|_{p+1,q} - 2f_i|_{p+2,q} + f_i|_{p+3,q})^2 + \frac{1}{4} (3f_i|_{p+1,q} - 4f_i|_{p+2,q} + f_i|_{p+3,q})^2. \quad (40)$$

Similarly, approximation of $f_i|_{p-\frac{1}{2},q}$ is carried out by considering appropriate stencils shown in Fig. 4 with respect to case I and case II. Further, the finite-difference WENO scheme does not require any special treatment in the case of 2D and 3D, in contrast to the finite-volume scheme methodology. Hence, the same methodology can be followed to compute the fluxes in y and z directions. Further, the calculation of gradient of distribution function in the y direction is similar and not covered due to brevity.

B. Additional dissipation and artificial viscosity terms

In the lattice Boltzmann simulation, the discretization process in time and space introduces both the dispersion and dissipation errors, and the collision term introduces a physical dissipation when the system deviates from the locally defined equilibrium. In order to avoid spurious local undershoots or overshoots in the simulation results, dissipation should be strong enough. It is observed that the model given by Kataoka and Tsutahara [22] is unstable when the Mach number exceeds 1, which implies the need for the dissipation term in order to overcome the numerical instability problem [26]. Hence, a dissipation term ($\lambda_i \frac{\partial^2 f_i}{\partial x_\beta^2}$) has been introduced to the above explained LBE method as

$$\frac{\partial f_i}{\partial t} + c_{i\beta} \frac{\partial f_i}{\partial x_\beta} - \lambda_i \left(\frac{\partial^2 f_i}{\partial x_\beta^2} \right) = \frac{1}{\epsilon} (f_i^{\text{eq}} - f_i), \quad (41)$$

where λ_i are constants independent of the physical space or time. The choice of the free parameter λ_i is one of the key tasks in these simulations. It is noted that the values of λ_i may not be same for all the benchmark cases. The choice may be guided by the dissipation error associated with the corresponding problem. Further, the discretization of the gradient term from Eq. (41) is expanded as

$$\frac{\partial f_i}{\partial x_\beta} = \frac{\partial f_i}{\partial x_\beta} + \beta_d \Delta x \left(\frac{\partial^2 f_i}{\partial x_\beta^2} \right). \quad (42)$$

The additional terms present on the right-hand side of Eq. (42) are artificial viscosity terms which help to reduce additional unphysical phenomena. Further, it is observed that the (β_d) terms are not enough to effectively improve the stability of the compressible LB simulation. In order to discretize the additional dissipation term from Eq. (41), a second-order central difference scheme is used. Further, it is important to

note that the macroscopic properties (3)–(5) derived from these additional terms may deviate from their Euler forms. However, these deviations can be minimized by controlling the pre-factors and coefficients present in these additional terms. Further, a detailed Chapman-Enskog analysis may be conducted in this regard. It should also be noted that the instabilities may also emerge from couplings between ghost and physical nodes [66,67]. However, such cases were not observed in the present study.

C. RK3 time integration

In order to achieve highly accurate time integration, multistage time-stepping methods, and oscillation-free scheme, the class of TVD (total variation diminishing) schemes are generally used. The TVD schemes were first developed for time-dependent gas dynamics. The scheme was able to establish monotonically preserving solution with a desirable property for a stable, nonoscillatory, higher order scheme. In order to achieve a monotonically preserving scheme, the total variation of the discrete solution should diminish with time. If the fifth-order WENO discretization is coupled with the first-order forward in time integration or the second-order Runge-Kutta time integration, then the solution is linearly unstable [50]. Hence, in the present study in order to avoid numerical instability, Runge-Kutta third-order time-stepping method is utilized as shown below:

$$\begin{aligned} f_i|_{p,q}^1 &= f_i|_{p,q}^n + \Delta t \mathcal{L}(f_i|_{p,q}^n), \\ f_i|_{p,q}^2 &= \frac{3}{4} f_i|_{p,q}^n + \frac{1}{4} f_i|_{p,q}^1 + \frac{1}{4} \Delta t \mathcal{L}(f_i|_{p,q}^1), \\ f_i|_{p,q}^{(n+\Delta t)} &= \frac{1}{3} f_i|_{p,q}^n + \frac{2}{3} f_i|_{p,q}^2 + \frac{2}{3} \Delta t \mathcal{L}(f_i|_{p,q}^2), \end{aligned} \quad (43)$$

where superscript (n) represents the n th time level and (1), (2), and (3) are intermediate time levels. \mathcal{L} is a spacial discretization operator, $n + \Delta t$ is the next time level, and Δt is the time step. In the case of the LBE method, \mathcal{L} is defined referring to Eq. (43) as below,

$$\mathcal{L} = -c_{i\beta} \frac{\partial f_i}{\partial x_\beta} \Big|_{p,q} + \lambda_i \left(\frac{\partial^2 f_i}{\partial x_\beta^2} \right) + \frac{f_i^{\text{eq}}|_{p,q} - f_i|_{p,q}}{\epsilon}. \quad (44)$$

D. Boundary conditions

The boundary conditions in the reported work are supersonic inflow, supersonic outflow, and reflective wall. This section briefly discusses the boundary condition implementation.

Supersonic inflow. Dirichlet boundary conditions are applied by specifying the macroscopic properties at the boundary. In the present LBE method, it is performed by

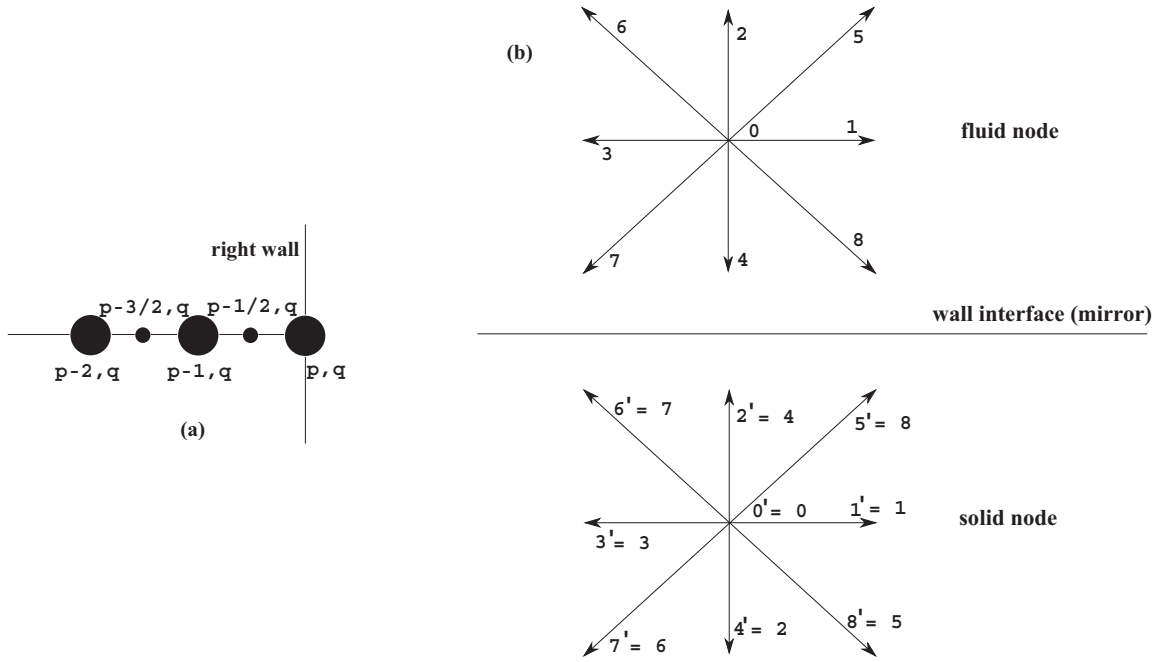


FIG. 5. Schematic of the boundary conditions: (a) supersonic outflow and (b) reflective boundary.

simply equating the distribution functions on the boundary nodes to the equilibrium distribution functions ($f_i = f_i^{\text{eq}}$), which are calculated for the given macroscopic properties using Eq. (20).

Supersonic outflow. The supersonic outflow boundary condition is implemented by considering the second-order gradient of the outflow nodes and the neighboring nodes to be equal. The calculation of the distribution functions at the right wall outlet node as shown in Fig. 5(a) is given below:

$$\text{grad}(f_i|_{p,q}) = \frac{3f_i|_{p,q} - 4f_i|_{p-1,q} + f_i|_{p-2,q}}{2\Delta x},$$

$$\text{grad}(f_i|_{p,q}) = \text{grad}(f_i|_{p-1,q}),$$

$$\text{therefore, } f_i|_{p,q} = \frac{4f_i|_{p-1,q} - f_i|_{p-2,q} + 2\Delta x \text{grad}(f_i|_{p-1,q})}{3.0}, \quad (45)$$

where $\text{grad}(f_i|_{p-1,q}) = \frac{\partial f_i}{\partial x}|_{p-1,q} = \frac{1}{\Delta x}(f_i|_{p-\frac{1}{2},q} - f_i|_{p-\frac{3}{2},q})$ is calculated by using the fifth-order WENO scheme.

Reflective boundary. The reflective boundary condition is implemented at the fluid-solid interfaces. The distribution functions at the solid nodes are assumed to be reflection of the values at the immediate fluid nodes. On the reflective bottom wall, two levels of ghost cells inside the wall are used as shown in Fig. 5(b) and their distribution functions (f_i), are determined by [68] following

$$f_i|_s = f_{i_{\text{mirror}}}|_{f_l}, \quad f_i|_{s-1} = f_{i_{\text{mirror}}}|_{f_{l+1}}. \quad (46)$$

Here, $f_i|_{f_l}$ and $f_i|_s$ represent the distribution functions at fluid nodes and solid nodes, respectively, and $f_{i_{\text{mirror}}}$ represent the distribution functions corresponding to the mirror direction of particle velocity direction i . However, it is to note that the boundary aligned distribution functions at

the solid node (i.e., $f_1|_s, f_0|_s, f_3|_s$) assume the same value of the distributions at the corresponding fluid node. The other distributions functions are reflected along the wall surface given by Eq. (46), e.g., ($f_5|_s = f_8|_{f_l}, f_2|_s = f_4|_{f_l}$), and ($f_5|_{s-1} = f_8|_{f_{l+1}}, f_2|_{s-1} = f_4|_{f_{l+1}}$). The distributions functions are computed at the second level of the ghost cells inside the wall, i.e., at location $(s-1)$, in order to obtain the gradients of the distributions using the fifth-order WENO described earlier.

III. RESULTS AND DISCUSSION

In this section, benchmark simulation results of widely studied one- and two-dimensional inviscid flow problems are given in detail. These benchmarks either have an exact (analytical) solution [69] or numerical results from the literature in order to compare with the simulation results obtained using the RK3 + WENO scheme presented in Sec. II. The first two problems are associated with minute and sudden changes in the fluid flow properties. The initial three problems are 1D and deal with abrupt changes in the flow properties, whereas the remaining ones depict high-speed flow containing oblique shocks. Here, one-dimensional lattice structure (see Fig. 1) is used to solve the first three benchmarks, while two-dimensional lattice structure (see Fig. 2) is used to solve the remaining ones.

A. The 1D Riemann problems

The first test problem is an initial value problem of the different physical parameters such as pressure, temperature, density, and velocity for gas with a discontinuous initial data, whose evolution is governed by the Euler equations. The 1D Riemann problems are commonly used for determining the accuracy of new solvers for inviscid supersonic flows.

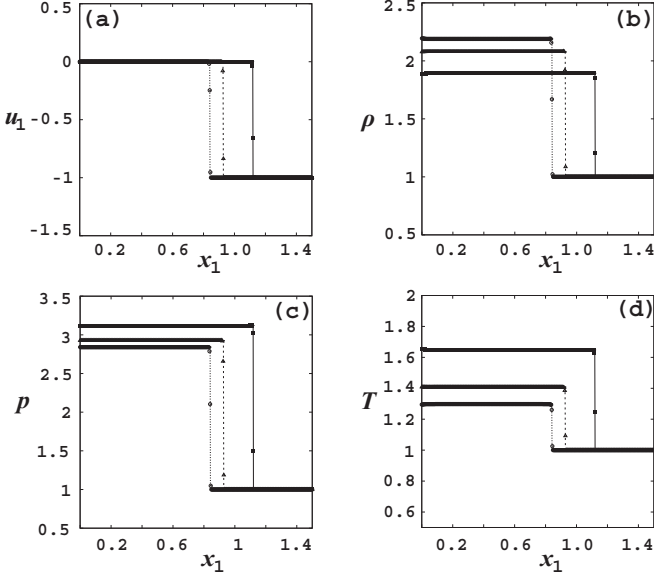


FIG. 6. The results of flow parameters (a) velocity, u_1 , (b) density, ρ , (c) pressure, p , and (d) temperature, T , by using RK3 + WENO LBE method for the shock-shock waves with Mach 1.0, $\Delta x = 0.002$, $\Delta t = 10^{-4}/4$. The simulation results are shown with by $\blacksquare = 5/3$; $\blacktriangle = 7/5$; and $\circ = 9/7$. The solid lines represents the results obtained by using analytical solutions [69] for $\gamma = 5/3$ (solid lines), $\gamma = 7/5$ (dashed lines), and $\gamma = 9/5$ (dotted lines). Since the results are symmetric about $x_1 = 0$, only the results for $x_1 > 0$ are shown.

In this subsection, various combinations of waves are studied for different boundary conditions to show the necessity of the additional terms discussed in Sec. II C. Initially, the shock-shock wave combination is simulated for three different initial conditions comprising inlet Mach numbers (1.0, 10.0, and 30.0). Further, the rarefaction-shock wave combination for three initial conditions with respect to low- and high-density ratios, sudden contact shock discontinuity, and shock-rarefaction wave combination for density ratio 5 are examined.

1. Shock-shock waves with low Mach number, $Ma = O(1)$

In order to solve problem involving initial inlet Mach number of 1.0 involving shock-shock wave combination, a one-dimensional lattice structure is utilized. The initial conditions are similar to those given in Ref. [22] and reproduced here:

$$\rho^0 = T^0 = 1, \quad u_1^0 = \begin{cases} 1 & \text{for } x_1 < 0; \\ -1 & \text{for } x_1 > 0. \end{cases} \quad (47)$$

In this work, for simulating Mach 1.0 flow the following parameters are utilized, namely, $v_1 = 1.0$ (equal to the given Mach number), $v_2 = 2.0$, and $\eta_0 = 1.5$. The numerical results for $t = 1$ and $\epsilon = 10^{-4}$ are compared with the analytical solution [69] for three values of $\gamma = 5/3$, $7/5$, and $9/7$ (or $b = 3, 5$, and 7 , respectively) as shown in Fig. 6.

2. Shock-shock waves with high Mach numbers, $Ma = O(10)$

In this subsection, two different high-Mach cases of 1D Riemann problem involving shock-shock wave combination

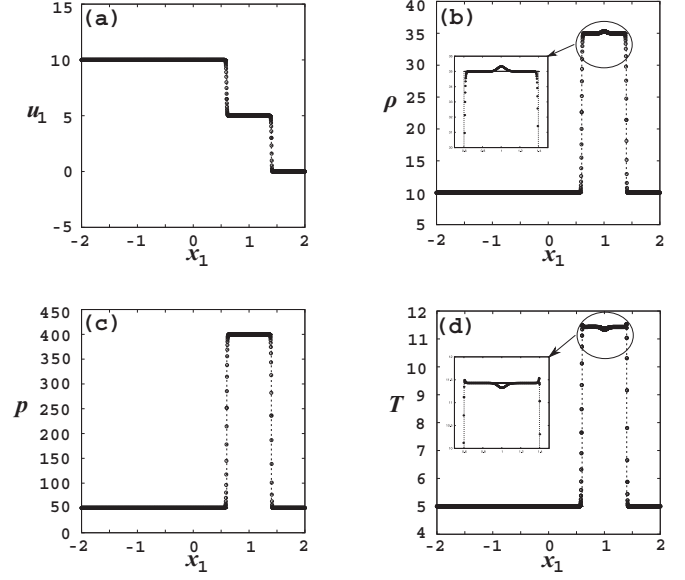


FIG. 7. The results of flow parameters (a) velocity, u_1 , (b) density, ρ , (c) pressure, p , and (d) temperature, T , by using RK3 + WENO LBE method for the shock-shock waves with Mach 10.0, $\Delta x = \Delta y = 0.002$, and $\Delta t = 10^{-4}$ at $t = 0.2$. The simulation results are shown with \circ whereas the dashed lines represent the result obtained by using analytical solution. The inner windows show the enlarged portion near the shock.

are detailed. The first case is simulated with Mach 10 and the other refers to Mach 30. Further, in order to solve the 1D problem involving high-Mach cases, a two-dimensional lattice structure is considered with three nodes in the y direction. The initial macroscopic variables at the left-hand and right-hand sides of the domain (represented using subscripts L and R) be ρ_L^0, p_L^0, u_L^0 , and ρ_R^0, p_R^0, u_R^0 , respectively.

$Ma = 10.0$. The initial conditions for this 1D Riemann problem are given by

$$\begin{aligned} (\rho^0, u_1^0, p^0)|_R &= (10.0, 0.0, 50.0) \quad \text{for } x \geq 0; \\ (\rho^0, u_1^0, p^0)|_L &= (10.0, 10.0, 50.0) \quad \text{for } x < 0. \end{aligned} \quad (48)$$

In this work, for simulating $Ma = 10.0$ flow following parameters are utilized, namely, $v_1 = 10.0$, $v_2 = 20.0$, $\eta_0 = 15.0$, $\beta_d = 0.25$, $\lambda_0 = v_1 dx$, $\lambda_{1-4} = 0.1 v_1 dx$, and $\lambda_{5-8} = 0$. The simulation results for $\gamma = 7/5$ are shown in Fig. 7 and compared with the analytical solution [69]. The results show wiggles-free solutions for this benchmark case justifying the case WENO approach. The values of β_d and λ_i governing the additional viscosity and dissipation terms, respectively, are indicated following Ref. [26].

$Ma = 30.0$. The initial conditions of the 1D Riemann problem are given below and refer to the test case in Ref. [26],

$$\begin{aligned} (\rho^0, u_1^0, p^0)|_R &= (7/5, 0.0, 1.0) \quad \text{for } x \geq 7.5; \\ (\rho^0, u_1^0, p^0)|_L &= (7/5, 30.0, 1.0) \quad \text{for } x < 7.5. \end{aligned} \quad (49)$$

In this work, for simulating $Ma = 30.0$ the following parameters are selected, namely $v_1 = 30.0$, $v_2 = 60.0$, $\eta_0 = 45.0$, $\beta_d = 0.25$, $\lambda_0 = v_1 dx$, $\lambda_{1-4} = 0.1 v_1 dx$, and $\lambda_{5-8} = 0$. The

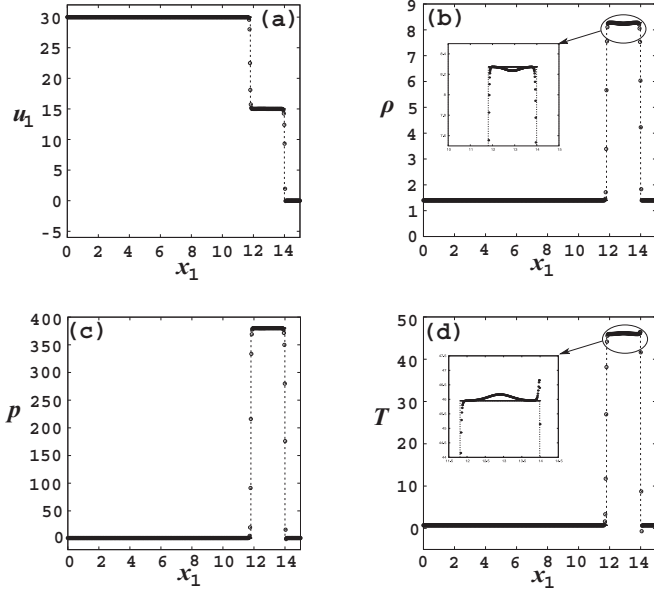


FIG. 8. The results of flow parameters (a) velocity, u_1 , (b) density, ρ , (c) pressure, p , and (d) temperature, T , by using the RK3 + WENO LBE method for the shock-shock waves with Mach 30.0, $\Delta x = \Delta y = 0.01$, and $\Delta t = 10^{-5}$ at $t = 0.36$. The simulation results are shown with \circ whereas the dashed lines represent the result obtained by using analytical solution. The inner windows show the enlarged portion near the shock.

simulation results for $\gamma = 7/5$ are shown in Fig. 8. From the figure, it is observed that the simulation results compare well with the analytical data [69].

B. Rarefaction-shock wave problem

In this subsection, the rarefaction-shock wave problem subjected to high-density ratios is examined using RK3 + WENO-based LBE.

1. Rarefaction-shock wave with high density ratio

$$(\rho^0|_L)/(\rho^0|_R) = 100 \text{ and } (\rho^0|_L)/(\rho^0|_R) = 1000$$

Two different high-density ratio cases for rarefaction-shock wave combination are solved using the RK3 + WENO LBE method in two dimensions with lattice structure as shown in Fig. 2 and the numerical results are detailed below.

$(\rho^0|_L)/(\rho^0|_R) = 100$. The initial conditions given in Ref. [70] are reproduced here:

$$u_1^0 = 0.0, \quad \rho^0 = \begin{cases} 100.0 & \text{for } x_1 < 0.5, \\ 1.0 & \text{for } x_1 \geq 0.5, \end{cases}$$

$$p^0 = \begin{cases} 100.0 & \text{for } x_1 < 0.5, \\ 1.0 & \text{for } x_1 \geq 0.5. \end{cases} \quad (50)$$

The model parameters are selected are $v_1 = 2.0$, $v_2 = 4.0$, $\eta_0 = 3.0$, $\beta_d = 0.25$, $\lambda_0 = v_1 dx$, $\lambda_{1-4} = 0.1 v_1 dx$, and $\lambda_{5-8} = 0$. The comparisons of the numerical results for $\gamma = 7/5$ are shown in Fig. 9. The discrepancies in the density and temperature plots (see Figs. 8 and 9) may be attributed to the assumption of v_1 equal to the inlet Mach number instead of $\sqrt{\gamma T} \text{Ma}$.

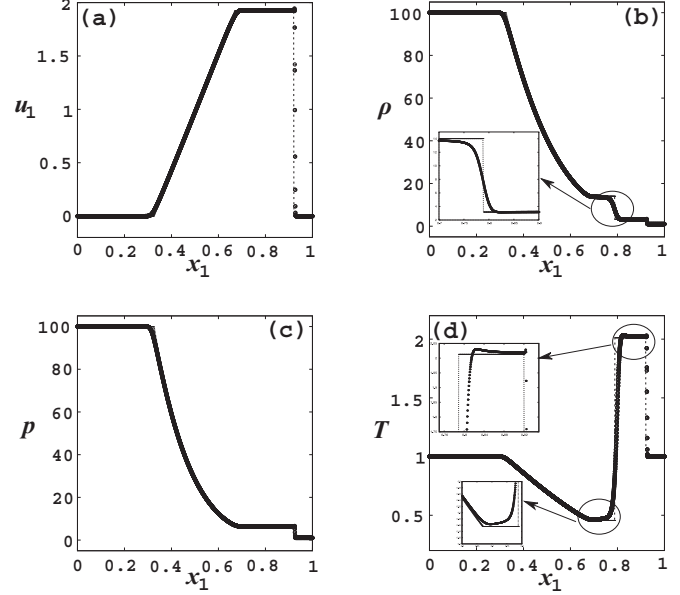


FIG. 9. The results of flow parameters: (a) velocity, u_1 , (b) density, ρ , (c) pressure, p , and (d) temperature, T , by using RK3 + WENO LBE method for rarefaction-shock waves with $(\rho^0|_L)/(\rho^0|_R) = 100$, $\Delta x = \Delta y = 0.0005$, $\Delta t = 10^{-4}$ at $t = 0.15$. The simulation results are shown with \circ , whereas, the dashed lines represent the analytical results. The inner windows show the enlarged portion near the shock.

$(\rho^0|_L)/(\rho^0|_R) = 1000$. The initial conditions given in Ref. [26] are reproduced here:

$$(\rho^0, u_1^0, p^0)|_L = (1000.0, 0.0, 1000.0) \text{ for } x < 7.5;$$

$$(\rho^0, u_1^0, p^0)|_R = (1.0, 0.0, 1.0) \text{ for } x \geq 7.5. \quad (51)$$

The model parameters are $v_1 = 3.0$, $v_2 = 6.0$, $\eta_0 = 4.5$, $\beta_d = 0.25$, $\lambda_0 = v_1 dx$, $\lambda_{1-4} = 0.1 v_1 dx$, and $\lambda_{5-8} = 0$. The simulation results for $\gamma = 7/5$ compare well with the analytical solution [69] (see Fig. 10). Further, in case of the high-density (refer Figs. 9 and 10) and high-Mach-number (see Figs. 7 and 8) simulation results, density and temperature profiles are not captured accurately. It is suspected that the deviation could be due to the discrete velocity model or lower number of grid points to capture the shock phenomena.

2. The 1D Riemann problem with stationary contact shock discontinuity, $(\rho^0|_L)/(\rho^0|_R) = 1.01$

The stationary contact discontinuity problem is examined using RK3 + WENO-based LBE method. The stationary contact discontinuity originates due to a sudden change in the parameter at some point in the domain. In order to investigate the problem involving sudden contact shock discontinuity for density ratio 1.01, the one-dimensional lattice model is utilized. The initial conditions are given by [70]

$$(\rho^0, u_1^0, p^0)|_L = (1.01, 0.0, 1.0) \text{ for } x < 0.5;$$

$$(\rho^0, u_1^0, p^0)|_R = (1.0, 0.0, 1.0) \text{ for } x \geq 0.5, \quad (52)$$

where the subscripts L and R represents the left- and right-hand sides of the discontinuity, respectively. In order to

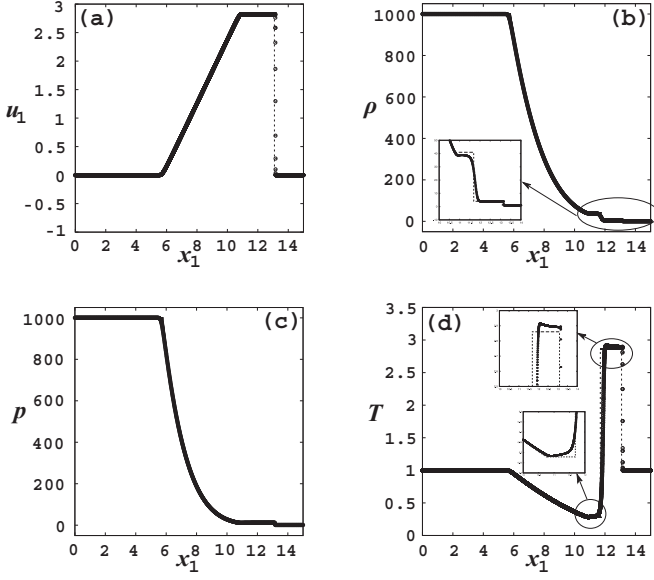


FIG. 10. The results of flow parameters (a) velocity, u_1 , (b) density, ρ , (c) pressure, p , and (d) temperature, T , by using RK3 + WENO LBE method for the rarefaction-shock waves with $(\rho^0|_L)/(\rho^0|_R) = 1000$, $\Delta x = 0.0025$, and $\Delta t = 2 \times 10^{-4}$ at $t = 1.5$. The simulation results are shown with \circ , whereas the dashed lines represent the analytical results. The inner windows show the enlarged portion near the shock.

simulate this problem, the flow parameters are selected as $v_1 = 1.0$, $v_2 = 2.0$, and $\eta_0 = 1.5$. The comparative results for u_1 , ρ , p , and T are shown in Fig. 11, wherein a negligible amount of overshoots and undershoots are seen (see the u_1 plot).

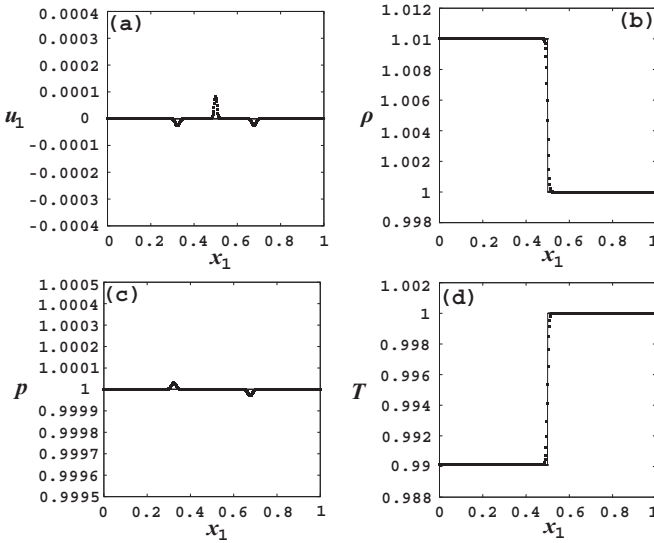


FIG. 11. The results of flow parameters (a) velocity, u_1 (b) density, ρ , (c) pressure, p , and (d) temperature, T , by using RK3 + WENO LBE method for the sudden contact shock discontinuity problem with $(\rho^0|_L)/(\rho^0|_R) = 1.01$, $\Delta x = 0.001$, and $\Delta t = 10^{-5}$ at $t = 0.15$. The simulation results are shown with \circ whereas, the dashed lines represent the analytical results.

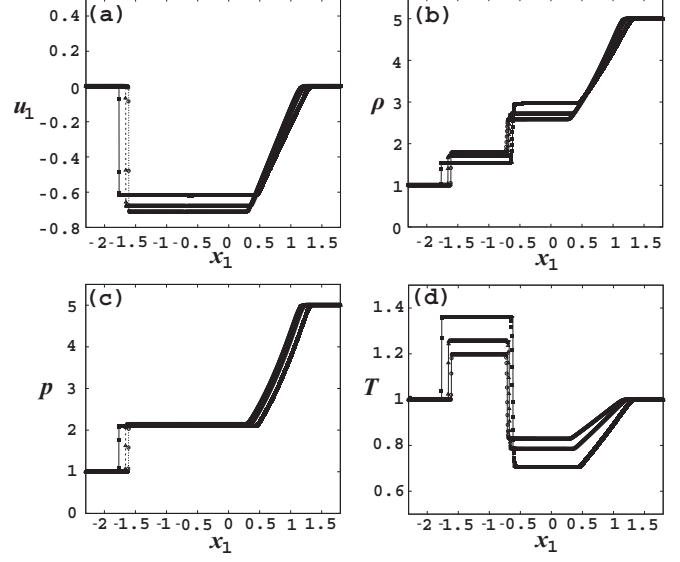


FIG. 12. The results of flow parameters (a) velocity, u_1 , (b) density, ρ , (c) pressure, p , and (d) temperature, T , using RK3 + WENO LBE method for shock-rarefaction wave with $\Delta x = 0.002$, $\Delta t = 10^{-4}/4$. The simulation results are shown with $\blacksquare = 5/3$; $\triangle = 7/5$; $\circ = 9/7$. The lines represent the results obtained by using analytical solutions for $\gamma = 5/3$ (solid lines), $\gamma = 7/5$ (dashed lines), and $\gamma = 9/5$ (dotted lines).

3. Shock-rarefaction waves problem

Here, the problem involving shock-rarefaction waves is detailed. The shock-rarefaction waves problem differs from the rarefaction-shock waves only with the change in the high-density region across the domain. The initial macroscopic properties given in Ref. [22] are $u_1^0 = 0$, $T^0 = 1$, $p_1^0 = 1$ for $x_1 < 0$, $p_1^0 = 5$ for $x_1 > 0$. In the simulations, $v_1 = 2.0$, $v_2 = 4.0$, and $\eta_0 = 3.0$ are considered. The numerical results at $t = 1$ and $\epsilon = 10^{-4}$ are compared for three values of $\gamma = 5/3$, $7/5$, and $9/7$ (or $b = 3$, 5 , and 7) with the analytical solutions as shown in Fig. 12.

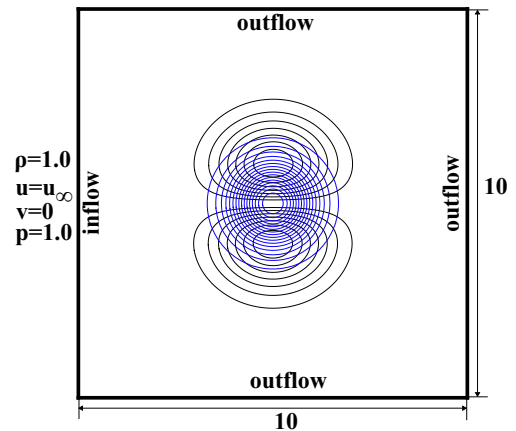


FIG. 13. A schematic for the isentropic vortex convection test. Blue and black colored lines respectively represent the isolines of pressure and $(u - u_\infty)/u_\infty$ in the initial condition.

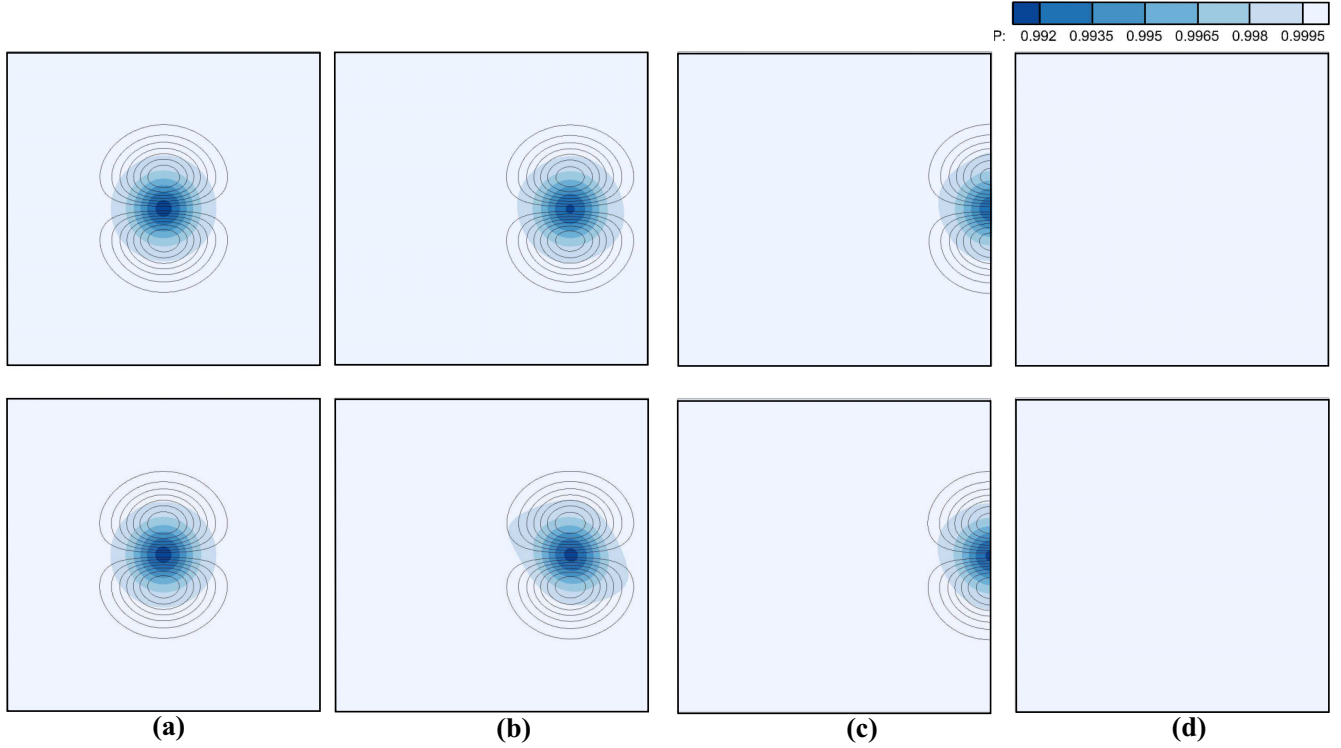


FIG. 14. Contour of the pressure field and isolines of $(u - u_\infty)/u_\infty$ in the isentropic vortex convection test. Top row shows the solution for inlet Mach number $Ma_\infty = 0.845$ at time (a) $t = 0$, (b) $t = 2.5$ (c) $t = 5$, and (d) $t = 10$. Bottom row is for the Mach number $Ma_\infty = 1.69$ at time (a) $t = 0$, (b) $t = 1.25$, (c) $t = 2.5$, and (d) $t = 5$.

C. Isentropic vortex convection test

An isentropic vortex convection test is performed to validate the outflow and nonreflecting boundary condition [71]. An isentropic vortex kept in the flow domain is allowed to move out of it through an outflow boundary which is under consideration. If the boundary condition is accurate (i.e., perfectly nonreflecting), then the vortex exits the domain in stipulated time without leaving any traces in the computational domain instead of spurious reflections. This test can also be used to qualitatively assess the extent of numerical viscosity values present in the solution. Inviscid flows do not generate vortices, nor do they effect vortices that are already present. Hence, in a numerical solution, the deformation of vortex signifies the addition of numerical viscosity by the flow solver.

In the present study, an isentropic vortex is kept at the center of a 10×10 square domain at $t = 0$ having a base flow ($\rho_\infty = 1$, $u_\infty = v_\infty = 0$, $p_\infty = 1$) as shown in Fig. 13. The initial condition for the problem is given as

$$\rho^0 = \left[1 - \frac{(\gamma - 1)b_v^2}{8\gamma\pi^2} e^{1-r^2} \right]^{\frac{1}{\gamma-1}}, \quad p^0 = \rho^\gamma, \quad (53)$$

$$u^0 = u_\infty - \frac{b_v}{2\pi} e^{\frac{1}{2}(1-r^2)} (y - y_c), \quad (54)$$

and

$$v^0 = \frac{b_v}{2\pi} e^{\frac{1}{2}(1-r^2)} (x - x_c), \quad (55)$$

where b_v is the strength of the vortex and $r = \sqrt{(x - x_c)^2 + (y - y_c)^2}$ is the distance from the center $(x_c, y_c) = (5, 5)$. For the present study, γ and b_v are chosen

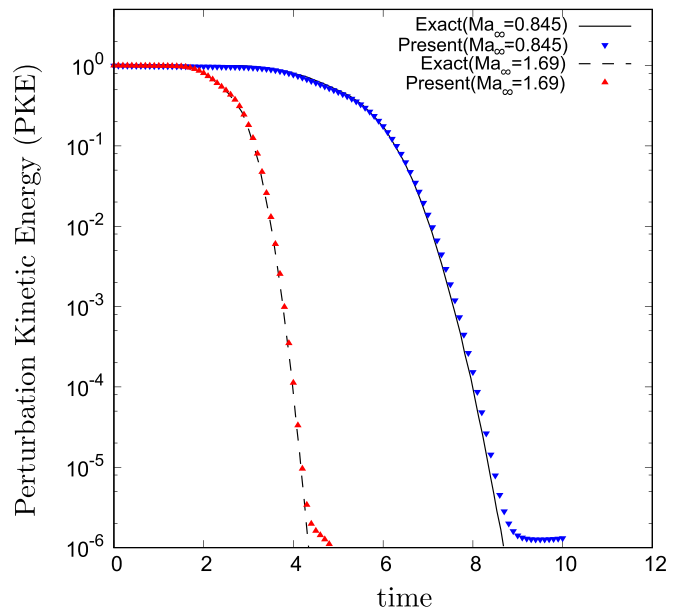


FIG. 15. Variation of normalized perturbation kinetic energy with time for inlet Mach numbers $Ma_\infty = 0.845$ and $Ma_\infty = 1.69$ compared with respective exact results.

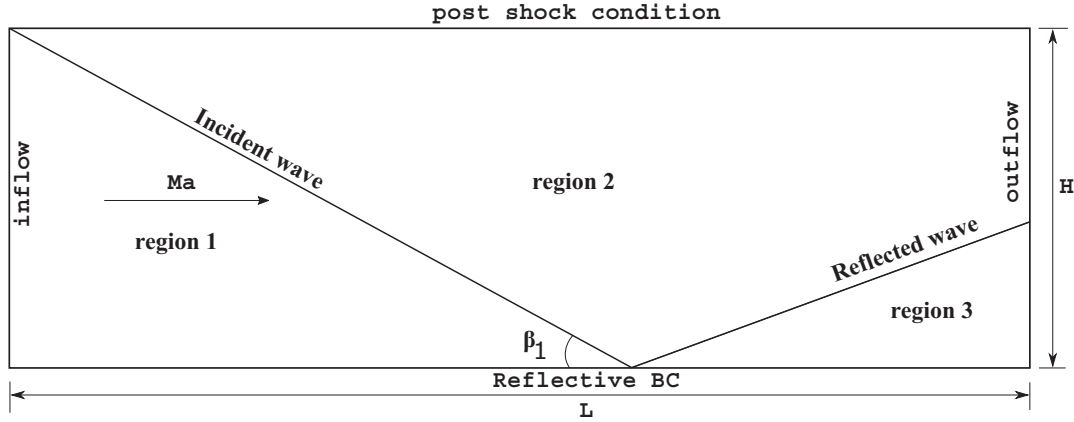


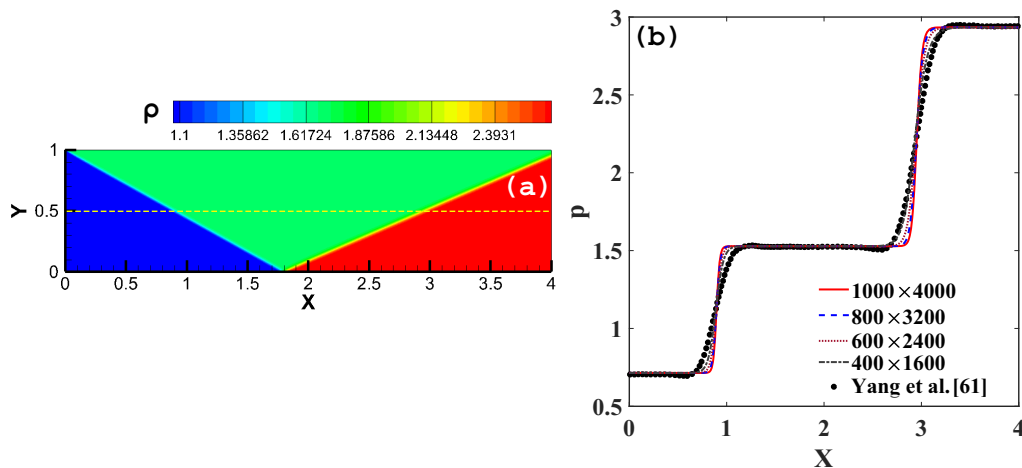
FIG. 16. A schematic for regular shock reflection.

to be $7/5$ and 0.5 respectively. Tests are conducted for inlet velocities $u_\infty = 1.0, 2.0$ (which correspond to Mach numbers $Ma_\infty = 0.845, 1.690$ respectively). v_1, v_2 , and η_0 for these simulations are chosen to be $Ma_\infty, 2Ma_\infty$, and $(v_1 + v_2)/2$ respectively. For the supersonic simulation (i.e., $Ma_\infty = 1.690$) dissipation ($\lambda_0 = v_1 dx$, $\lambda_{1-4} = 0.1v_1 dx$, and $\lambda_{5-8} = 0$) and artificial viscosity ($\beta_d = 0$) are added. For the $u_\infty = 1$ flow, it is expected that 50% of the vortex is moved out of the domain in 5 time units and 100% in 10 time units, without leaving any traces behind in the computational domain. For the $u_\infty = 2$ flow, similar phenomenon is expected at 2.5 and 5 time units respectively. Figure 14 (top row) shows the pressure contour and isolines of $(u - u_\infty)/u_\infty$ at time $t = 0, 2.5, 5$, and 10 respectively, for $Ma_\infty = 0.845$ and Fig. 14 (bottom row) shows the same for $Ma_\infty = 1.69$ at time $t = 0, 1.25, 2.5$, and 5. Small amount of vortex distortion can be seen in the $Ma_\infty = 1.69$ case [see Fig. 14 (bottom row)], which perhaps is caused due to the use of additional terms. For the quantitative measure of spurious reflections, average perturbation kinetic energy (PKE) defined as $[(u - u_\infty)^2 + (v - v_\infty)^2]/2$ is computed for each time step. Figure 15 shows time evolution of average

PKE normalized by initial average PKE. It is evident from Figs. 14 and 15 that the spurious reflections from outflow boundary are minimal.

D. Regular shock reflection

Here, a regular shock reflection off a flat boundary (or plate) is detailed. This problem statement is commonly used for validating the numerical scheme. The high-speed flow encounters a wedge, and depending on the wedge angle various reflection phenomena are observed. The regular shock reflection occurs when the wedge angle is less than the maximum possible wedge angle in order to obtain an oblique shock solution. In the present work, the regular shock reflection is simulated inside a two-dimensional computational domain with the similar boundary conditions for two representative inlet Mach numbers. The first case deals with a inlet Mach of 2.9, for which quantitative results available in the literature are used to compare the density variation. The second problem is associated with the 10.0 Mach at the inlet. The simulation results are compared with the analytical solution for which the procedure is shown in the Appendix. The boundary conditions

FIG. 17. Regular shock reflection: (a) contour plot of density and (b) pressure variation profile along the x at $y = 0.5$ for varying grid sizes at 2.9 Ma number.

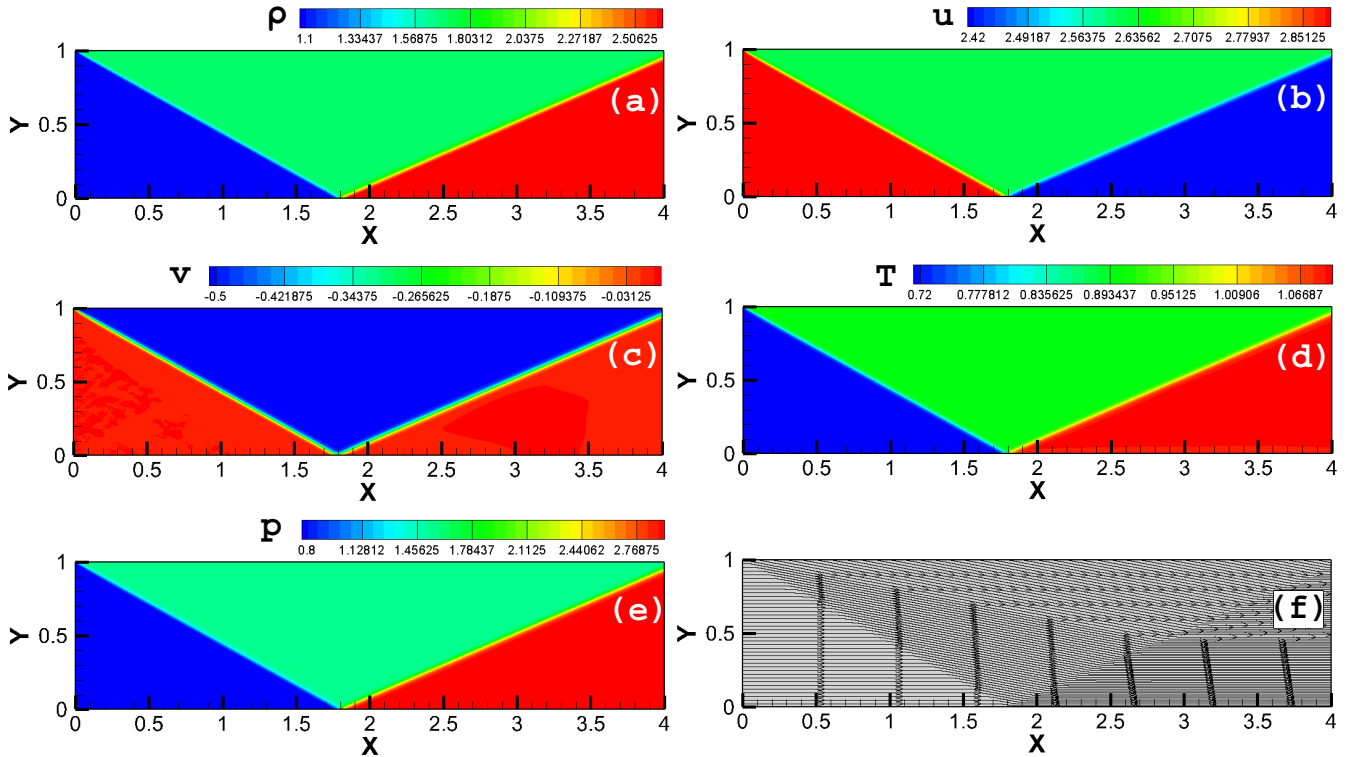


FIG. 18. Regular shock reflection flow properties for $Ma = 2.9$, $\Delta x = \Delta y = 1.0/1000$, $\Delta t = 5.172 \times 10^{-5}$, and $t = 3.5$, with contour plots of (a) density, ρ , (b) x -direction velocity, u , (c) y -direction velocity, v , (d) temperature, T , (e) pressure, p , and (f) streamlines plot.

used for solving the regular shock reflection are composed of a reflective surface along the bottom boundary, supersonic outflow along the right boundary, and Dirichlet conditions are applied at the inlet and the top boundary (i.e., postoblique shock state) of the domain. At the beginning, the solution of the entire domain is set to be that at the left boundary. The computational domain with a length $L = 4$ units and height, $H = 1$ units along with the boundary conditions is shown as schematic in Fig. 16.

1. Regular shock reflection with inlet Mach 2.9

A shock with a shock wave angle of 29° and a preshock Mach 2.9 reflects off a flat plate. The left boundary is set at an inflow with $u = Ma = 2.9$, in the positive x direction. The Dirichlet boundary conditions on the left-hand and top sides

of the domain as in Ref. [72] are given below,

$$\begin{aligned}
 (\rho, u, v, p)|_{\text{left}} &= (1.0, 2.9, 0.0, 5.0/7.0); \\
 (\rho, u, v, p)|_{\text{top}} &= (1.69997, 2.6934, -0.50633, 1.52819).
 \end{aligned}
 \tag{56}$$

In order to simulate the regular shock reflection corresponding to the inflow $Ma = 2.9$ the following parameters are utilized, namely, $v_1 = 2.9$, $v_2 = 5.8$, $\eta_0 = 4.35$, $\beta_d = 0.25$, $\lambda_0 = v_1 dx$, $\lambda_{1-4} = 0.1 v_1 dx$, and $\lambda_{5-8} = 0$. The contour plot with 30 equally spaced density contours in the range $1.1 < \rho < 2.6$, at time $t = 3.5$ using a uniform grid size of 1000×4000 is shown in Fig. 17(a). The quantitative comparisons with the result given in Ref. [61] are shown in Fig. 17(b) considering various grid sizes. The increase in the grid sizes allows for a sharp changes in the flow properties without numerical oscillations. It is observed that the lower grid sizes would generate the hyperbolic tangent profile as given in Ref. [61]; however, in this article fine resolution is followed

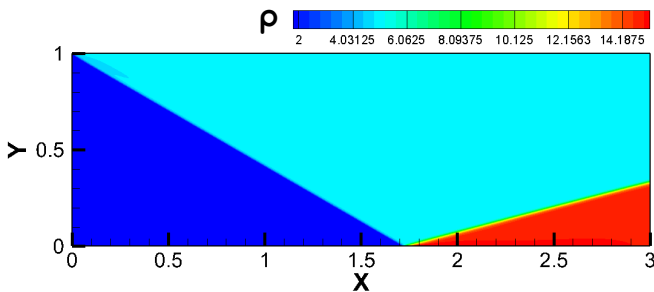


FIG. 19. Regular shock reflection: density contours for $Ma = 10.0$ at time $t = 0.6$.

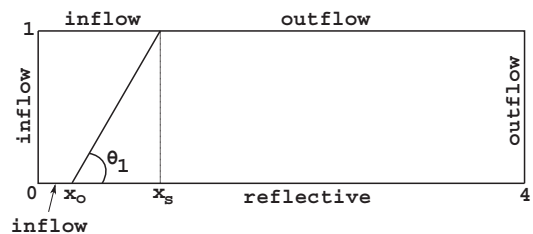


FIG. 20. Schematic of double Mach reflection (DMR) benchmark.

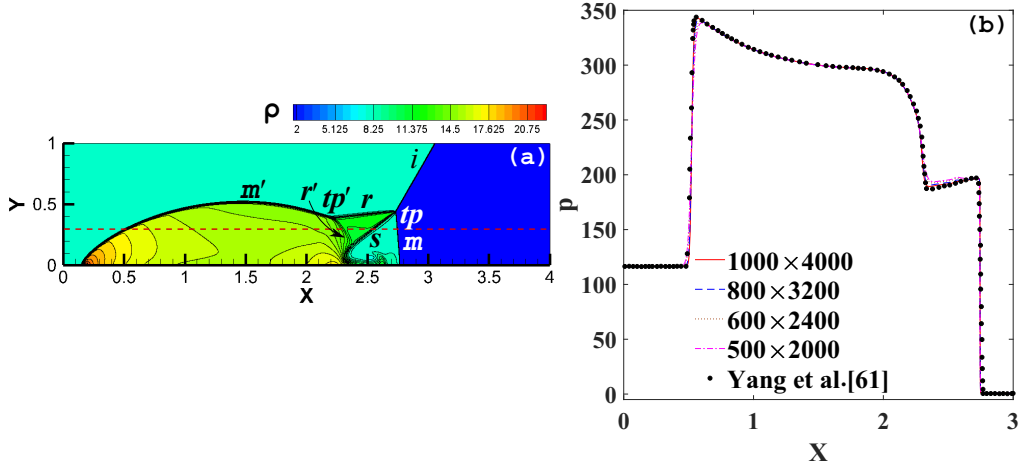


FIG. 21. Double Mach reflection: (a) contour plot of density and (b) pressure variation profile along the x direction at $y = 0.3$ by using various grid sizes at $Ma = 10.0$.

for all the benchmark simulation studies. Further, the dissipation error near to the discontinuity is reduced with an increase in the grid size. The physical properties such as density, x -direction velocity, y -direction velocity, temperature, and pressure all with equally spaced contours as well as the streamline patterns at $t = 3.5$ are shown in Fig. 18. The simulation results are also compared with an analytical solution discussed in the Appendix. The region ① represents the portion before the incident shock, region ② is a space between the incident and the reflected shock, and region ③ is a

portion after the reflected shock. The supersonic inviscid flow properties, namely, ρ , x -direction velocity (u), y -direction velocity, pressure (p), and temperature (T), are measured in each region and a comparison with the analytical solution is presented subsequently. The flow parameters are measured at a point (0.5, 0.5) in region ①, (1.75, 0.5) in region ②, and (3.5, 0.5) in region ③, respectively. The simulation results in the region ① measure $\rho = 1.0$, $u = 2.9$, $v = 0.0$, $p = 0.7143$ and $T = 0.7143$. Similarly, in the region ②, $\rho = 1.699$, $u = 2.62$, $v = -0.506$, $p = 1.528$, and $T = 0.899$ and in region

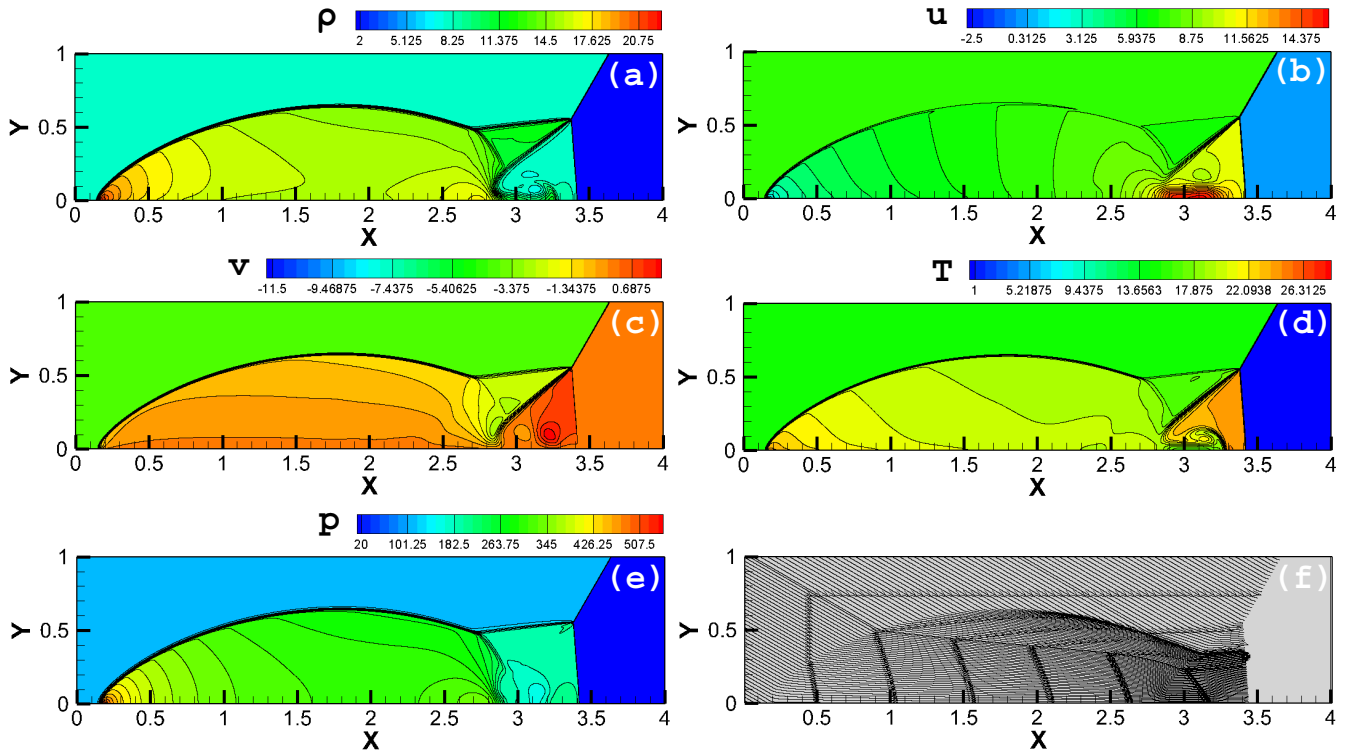


FIG. 22. Double Mach reflection flow properties: $Ma = 10.0$, $\Delta x = \Delta y = 1.0/1000$, $\Delta t = 3.5 \times 10^{-6}$, and for $t = 0.25$, contour plots of (a) density, ρ , (b) x -direction velocity, u , (c) y -direction velocity, v , (d) temperature, T , (e) pressure, p , and (f) streamlines plot.

③, $\rho = 2.684$, $u = 2.40$, $v = 0.0$, $p = 2.934$, and $T = 1.093$. The analytical results closely match with the simulation results with less than 0.1% error.

2. Regular shock reflection with inlet Mach 10.0

The computational domain considered is of length 3 units and height 1 unit with the boundary conditions as shown in Fig. 16. An oblique shock with a shock wave angle of 30° , preshock Mach number of 10 reflects off a flat plate. The left boundary is kept as inflow with $u = \text{Ma} = 10.0$ in the positive x direction, $\rho = 1.0$, $p = 7.0/5.0$. The boundary conditions on the left-hand and top sides are as per Ref. [26],

$$\begin{aligned} (\rho, u, v, p)|_{\text{left}} &= (1.0, 10.0, 0.0, 5.0/7.0); \\ (\rho, u, v, p)|_{\text{top}} &= (5.0, 8.0, -3.4641, 20.7143). \end{aligned} \quad (57)$$

Further, the model parameters for the regular shock reflection with an inflow of $\text{Ma} = 10.0$ are given as $v_1 = 10.0$, $v_2 = 20.0$, $\eta_0 = 15.0$, $\beta_d = 0.25$, $\lambda_{0-4} = 0.6v_1 dx$, and $\lambda_{5-8} = 0$. The contour plot with 30 equally spaced density contours in the range $2.0 < \rho < 15.0$ using 1000×3000 grids at time $t = 0.6$ is shown in Fig. 19. The analytical solution as discussed in Appendix is used for the comparison with the simulation results. The flow properties are measured in each region and values are compared with the analytical solution. The measurements are performed at points (1.0, 0.2) in region ①, (1.7, 0.2) in region ②, and (2.8, 0.2) in region ③, respectively. The simulation results in region ① measures $\rho = 1.0$, $u = 10.0$, $v = 0.0$, $p = 0.7143$, and $T = 0.7143$. Similarly, in region ②, values of $\rho = 4.95$, $u = 7.99$, $v = -3.46$, $p = 20.716$, and $T = 4.186$ are attained. In region ③, $\rho = 14.9$, $u = 7.11$, $v = 0.0$, $p = 116.14$, and $T = 7.79$ are estimated. The simulation results closely matches with the analytical solution with less than 1% error.

E. Double Mach reflection (DMR)

The double Mach reflection (DMR) is inspired by experimental and numerical studies on reflections of planar shocks in the air from the wedge [60]. The problem is set up experimentally by driving a shock down a tube containing a wedge. In the beginning, a simple planar shock meets the wall of the tube at right angles; however, as the wall begins to slope, complicated shock reflection structures are seen. A self-similar flow develops at this point which can be parameterized for a given ideal gas and the inflow Mach number over the wedge. The problem is initially compared with a line plot with the inflow Mach number of 10.0 and the wedge angle as 30° . Later, in order to understand the difference between the attached and detached shock patterns, a 40° wedge angle is chosen from the possible DMR solution for diatomic gas [73]. The extension is carried out for an inflow Mach number of 6 with two wedge angles (30° and 40°) in order to determine the effect of change in the Mach number and the wedge angle on the flow or shock structures.

The computational domain considered for the DMR benchmark is as shown in Fig. 20. The reflecting wall lies along the bottom of the computational domain, beginning at $x_0 = 1/6$. The angle of the corner is represented as θ and to avoid the complications of simulation for the inclination of the geom-

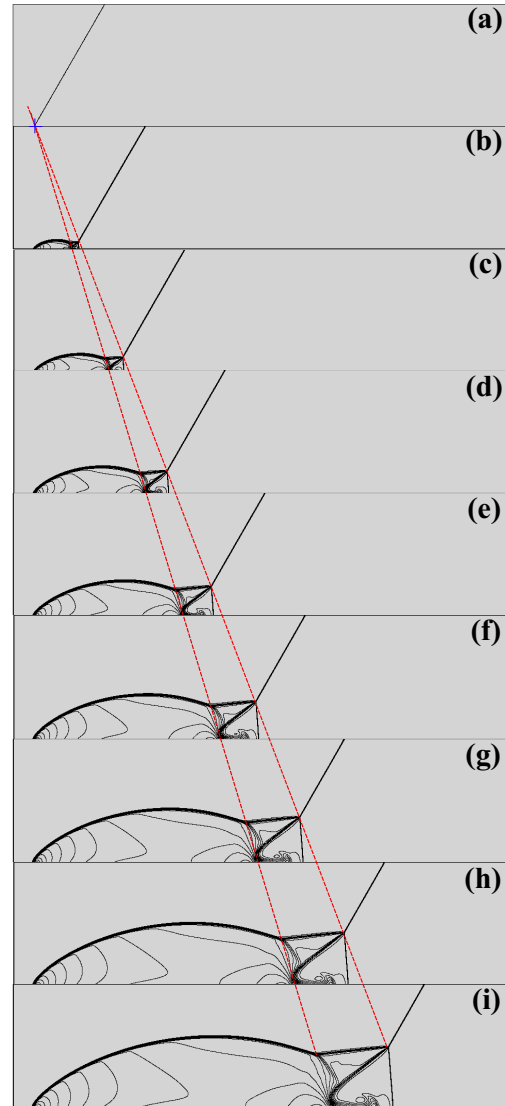


FIG. 23. Growth of self-similar solution between $t = 0$ and $t = 0.224$; plots (a) through (i) represent isopycnics with equal time interval of $t = 8000\Delta t$ (where, $\Delta t = 3.5 \times 10^{-6}$) between $t = 0$ to $t = 0.224$. The lines follow the trajectory of the two triple points.

etry, an inclined wall is taken as horizontal (coinciding with x direction) and the incident shock is turned by an angle, θ . A shock with angle $\theta_1 = \pi/2 - \theta$ and inflow Mach number (Ma) moves through a still air mass with $\gamma = 7/5$, $\rho = 7/5$, and $p = 1.0$. The shock reaches an apex ($x_0, 0$) of the wedge at $t = 0$ and the postshock state is determined by using the Rankine-Hugoniot jump conditions. The left-hand boundary is set at an inflow condition. A supersonic outflow condition is applied for the bottom boundary portion corresponding to $x < x_0$ and the right-hand side boundary. Further, the upper boundary condition is set to follow the shock as the shock moves to the right of the domain. The interaction point between the shock and the upper boundary moves at a speed of $|u_s|/\cos\theta$ and is located at $x_s(t) = x_0 + y \tan\theta + t|u_s|/\cos\theta$. Next, the flow structures for two different Mach numbers with wedge angle variation are discussed.

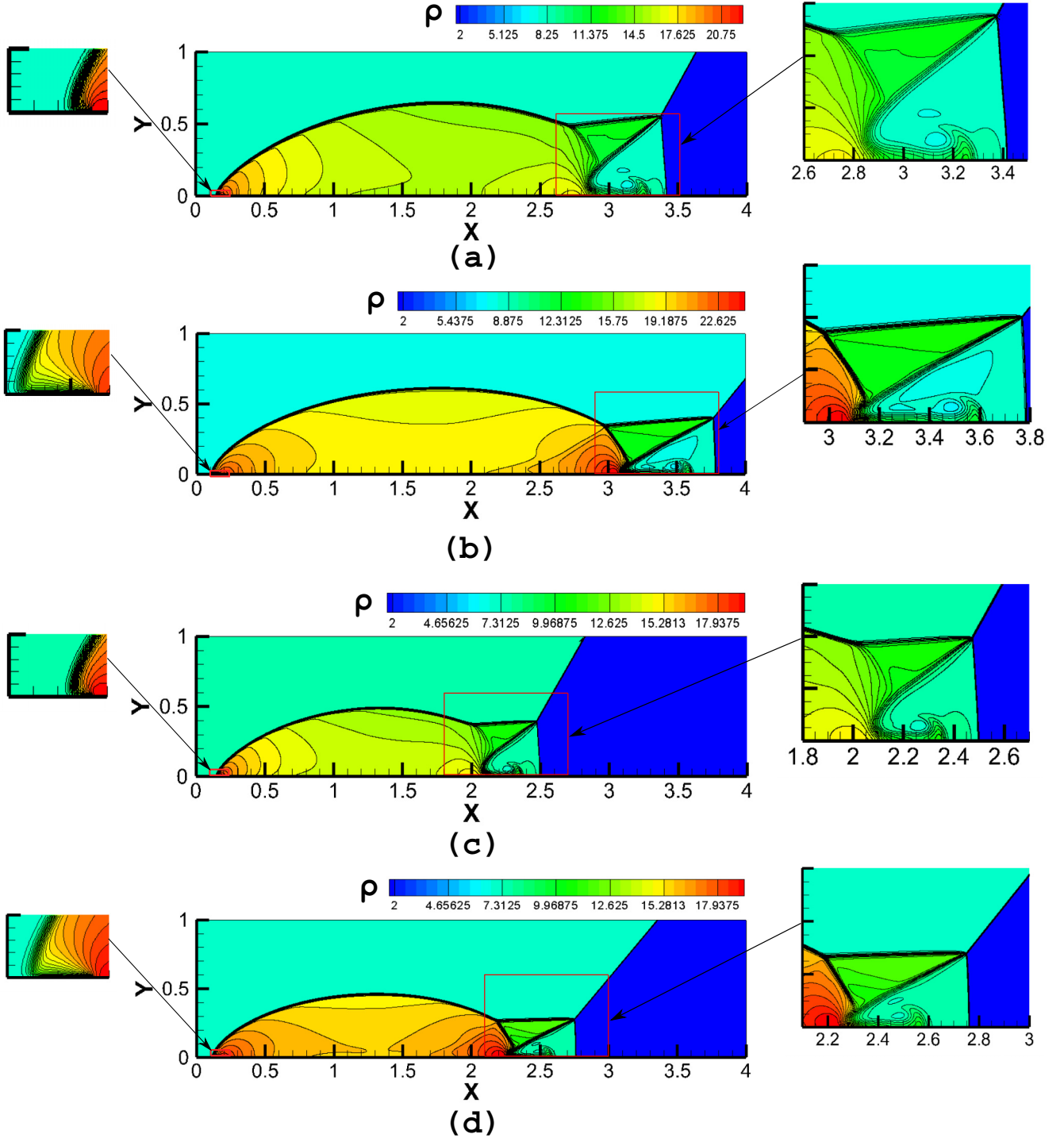


FIG. 24. Plot of density with equally spaced contours: (a) $Ma = 10, \theta = 30^\circ$, (b) $Ma = 10, \theta = 40^\circ$, (c) $Ma = 6, \theta = 30^\circ$, and (d) $Ma = 6, \theta = 40^\circ$; with enlarged portions near the $(x_0, 0)$ location and the triple-point shock systems.

1. DMR with inflow $Ma = 10$, wedge angle of $\theta = 30^\circ$

In this section, the conventional benchmark followed in the literature involving inflow of 10 Mach with a wedge angle of $\theta = 30^\circ$ is detailed. The initial conditions are given by

$$\begin{aligned} x &> x_0 + y \tan \theta, & x < x_0 + y \tan \theta; \\ u &= 0.0, & u = 8.25 \cos \theta; \\ v &= 0.0, & v = -8.25 \sin \theta; \end{aligned}$$

$$\begin{aligned} \rho &= 7/5, & \rho &= 8.0; \\ p &= 1.0, & p &= 116.5. \end{aligned} \quad (58)$$

The inflow condition at the left-hand boundary, the bottom boundary portion ($x < x_0$), and the top boundary portion ($x < x_s(t)$; for $y = 1.0$) corresponds to the flow properties given in Eq. (58) for $x < x_0 + y \tan \theta$. Next, the simulation parameters for DMR with an inflow of $Ma=10.0$ and

wedge angles (30° and 40°) are selected as $v_1 = 10.0$, $v_2 = 20.0$, $\eta_0 = 15.0$, $\beta_d = 0.25$, $\lambda_0 = v_1 dx$, $\lambda_{1-4} = 0.2v_1 dx$, and $\lambda_{5-8} = 0$. The plot with 33 equally spaced density contours in the range $7/5 < \rho < 22.0$ with an uniform grid size of 1000×4000 at time $t = 0.20$ is shown in Fig. 21(a). The simulation results are compared with results from the literature [61] for pressure variation profile along the x direction at $y = 0.3$ by using various grid sizes at time $t = 0.20$, as shown in Fig. 21(b). It is observed that near to the sudden discontinuity with an increase in the grid size the dissipation error is reduced. The benchmark flow or shock structure for the DMR case is briefly discussed. The first triple point (tp) system consists of the incident shock wave (i), the reflected shock wave (r), and the Mach stem (m). In the literature, these features are observed to be sharp (or thin), whereas the contact discontinuity or the first slip-stream (s) features diffusion effects as seen in Fig. 21(a). Further, in the case of the second triple point (tp') system, the incident shock wave ($i' = r$) and the second Mach stem (m') are sharp. However, diffusional effects are observed at the reflected shock (r'). The latter features a minute deviation from a continuous curvature when it reaches the first slip stream (s). The instability at the first slip stream between regions of the primary Mach-stem and the reflected shock wave from the first triple point has not been reproduced in this work. The growth of instability at the first slip stream may be due to secondary turbulent mixing [74]. The second slip stream (s') is not noticeable in the current simulation results. The difficulty in the resolution of these features numerically and experimentally are well known [46,58].

Further, the physical properties such as density, x -direction velocity, y -direction velocity, temperature, and pressure with equally spaced contours, along with the streamline patterns at $t = 0.2$ are shown in Fig. 22. Furthermore, the constant density contours (isopycnics) from $t = 0$ to $t = 0.224$ are shown in Fig. 23 wherein the growth of self-similar solution has been depicted through the plots [see Figs. 23(a) through 23(i)]. The locations of primary and secondary triple-point systems with respect to time are joined with lines and it is observed that these triple-point locations pass through two dotted lines at each time interval and the dotted lines should intersect at the point $(x_0, 0)$ as shown in Fig. 23, suggesting the accuracy in the time evolution of the shock structure [75].

2. DMR problem with $Ma = 6$, wedge angles of $\theta = 30^\circ$ and 40°

In this section, the new results for double Mach reflection with inlet Mach 6.0 and wedge angles of 30° and 40° are detailed. The initial conditions for both the problems are the same except for the wedge angle, represented as θ . The initial conditions are defined as

$$\begin{aligned} x &> x_0 + y \tan \theta, & x < x_0 + y \tan \theta; \\ u &= 0.0, & u = 4.86 \cos(\theta); \\ v &= 0.0, & v = -4.86 \sin(\theta); \\ \rho &= 7/5, & \rho = 7.3759; \\ p &= 1.0, & p = 41.833. \end{aligned} \quad (59)$$

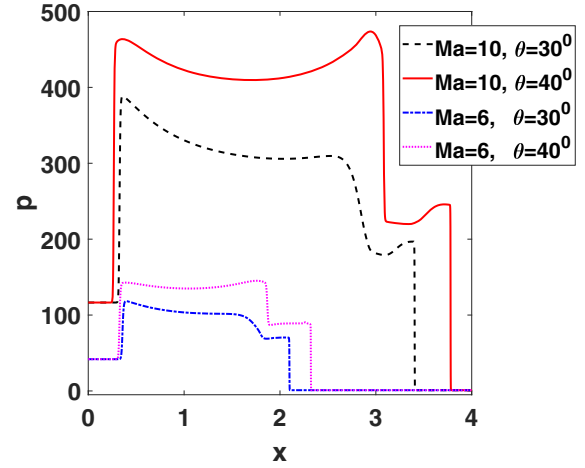


FIG. 25. Comparison of pressure variation profile along the x direction at $y = 0.2$, time, $t = 0.25$ for various inflow Mach numbers, and wedge angles of DMR problem.

Further, the following parameters are selected, namely, $v_1 = 6.0$, $v_2 = 12.0$, $\eta_0 = 9.0$, $\beta_d = 0.25$, $\lambda_0 = v_1 dx$, $\lambda_{1-4} = 0.2v_1 dx$, and $\lambda_{5-8} = 0$. The plots of density with 30 equally spaced contours in the range of $7/5 < \rho < 20.0$ obtained using uniform grids of 1000×4000 at time $t = 0.25$ for different wedge angles and two Mach numbers are shown in Fig. 24. Here, the plots in Figs. 24(a) and 24(b) represent results for $Ma = 10.0$ with $\theta = 30^\circ$ and $\theta = 40^\circ$, respectively, while those in Figs. 24(c) and 24(d) depict the density contours for $Ma = 6.0$ with $\theta = 30^\circ$ and $\theta = 40^\circ$, respectively. The enlarged portions near the $(x_0, 0)$ location and the triple-point shock systems are also plotted. It is observed that with the increase in the wedge angle the contour lines shift toward the left of the domain near the $(x_0, 0)$ location. Further, from the shock diffraction domain [75], it can be inferred that the detached shock pattern is observed in all the presently studied cases except in the case of $Ma = 10$ with $\theta = 30^\circ$. The comparison between the contour plots of density for different inlet Mach number and wedge angle can be easily made from Fig. 24. It is inferred that the pressure and density value increases with the increase in the wedge angle. The changes can be observed in the Mach stems location and height, triple-point location, and distance traveled by the shock and the other flow or shock structures. From the enlarged portion, one can conclude regarding attached and detached shock (especially

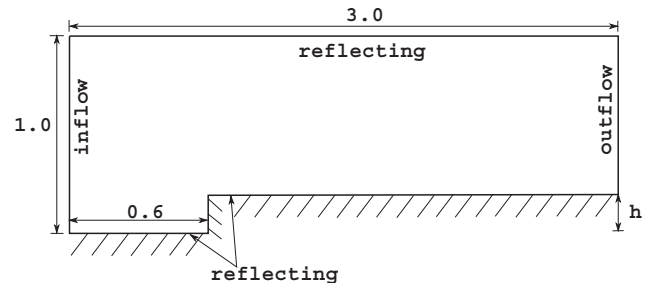


FIG. 26. Schematic of supersonic inviscid flow over a forward-facing step: computational domain and boundary conditions.

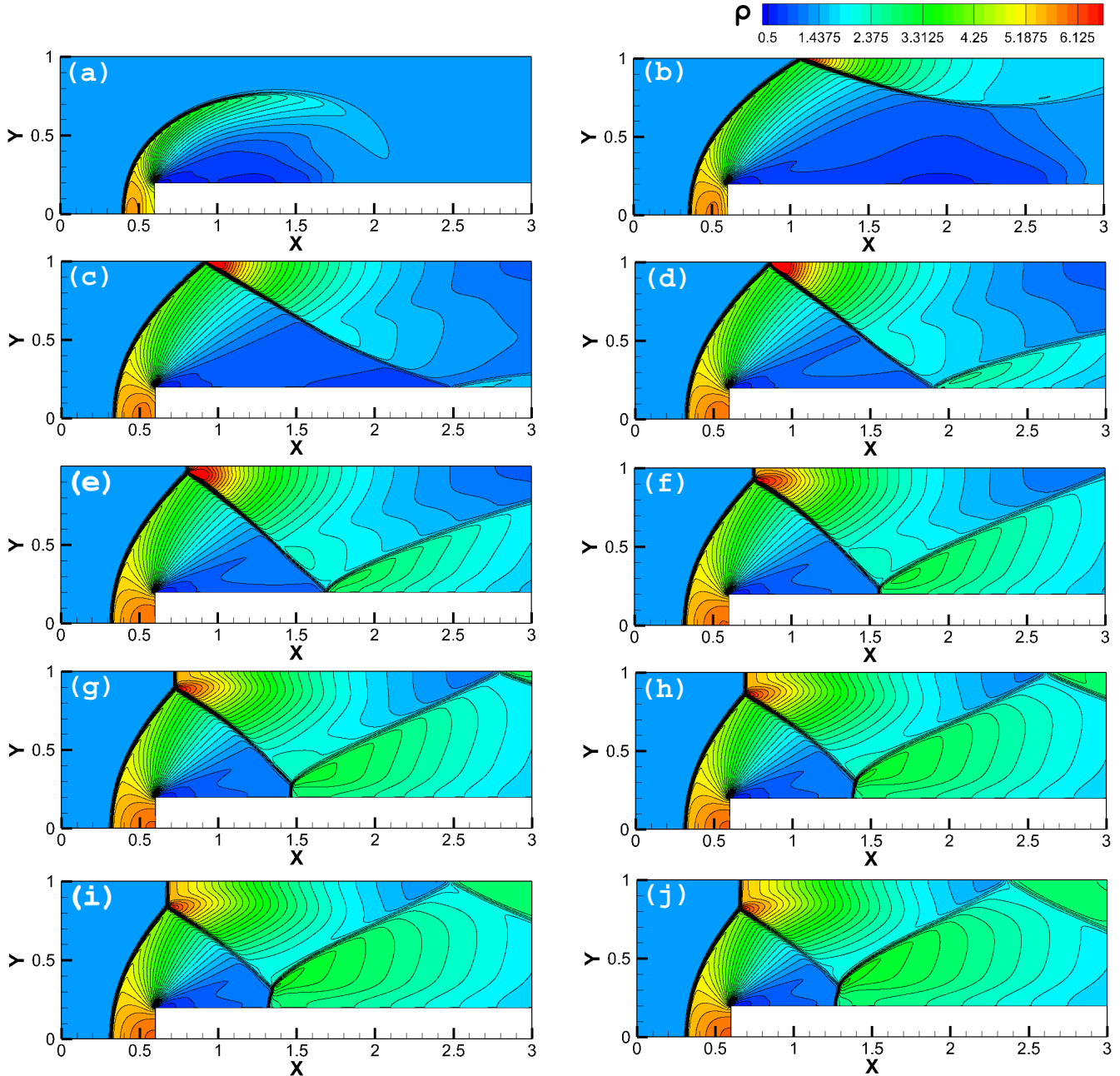


FIG. 27. Flow structure with shock for supersonic inviscid flow over a forward-facing step: transient flow solutions at various times, t ; $\text{Ma} = 3.0$, step-height = 0.2, $\Delta x = 1.0/1000$, $\Delta t = 5 \times 10^{-5}$, and 33 density contours in the range of $0.5 < \rho < 6.5$, for (a) $t = 0.4$; (b) $t = 0.8$; (c) $t = 1.2$; (d) $t = 1.6$; (e) $t = 2.0$; (f) $t = 2.4$; (g) $t = 2.8$; (h) $t = 3.2$; (i) $t = 3.6$; and (j) $t = 4.0$.

for inlet Mach number 10.0). The detached shock is formed at the beginning of the reflecting wall at $x = x_0$ for the wedge angle of 40° ; see Fig. 24(b). The initial conditions for realizing Fig. 24(b) are given in Eq. (58). Further, the comparison of pressure variation profile along the x direction at $y = 0.2$, time, $t = 0.25$ for various inflow Mach numbers and wedge angles of DMR problem is shown in Fig. 25. Finally, the DMR can be classified into three different subtypes such as positive double Mach reflection (DMR^+), negative double Mach reflection (DMR^-), and transitional DMR, depending on the trajectory angle of the primary and the secondary triple point with respect to the wedge [58]. In the present study, it is found

that the trajectory angle of the secondary triple point is greater than the primary triple point, also known as the DMR^+ .

F. Forward-facing step problem

In this section, widely studied two-dimensional benchmark problem of a supersonic inviscid flow over forward-facing step [60] has been detailed. The problem statement encompasses an uniform flow of a constant Mach at the inlet of a channel (also referred as “wind tunnel” in the literature) with a step of particular height and at a particular distance from the inlet. Initially, for the validation purpose, the inlet Mach

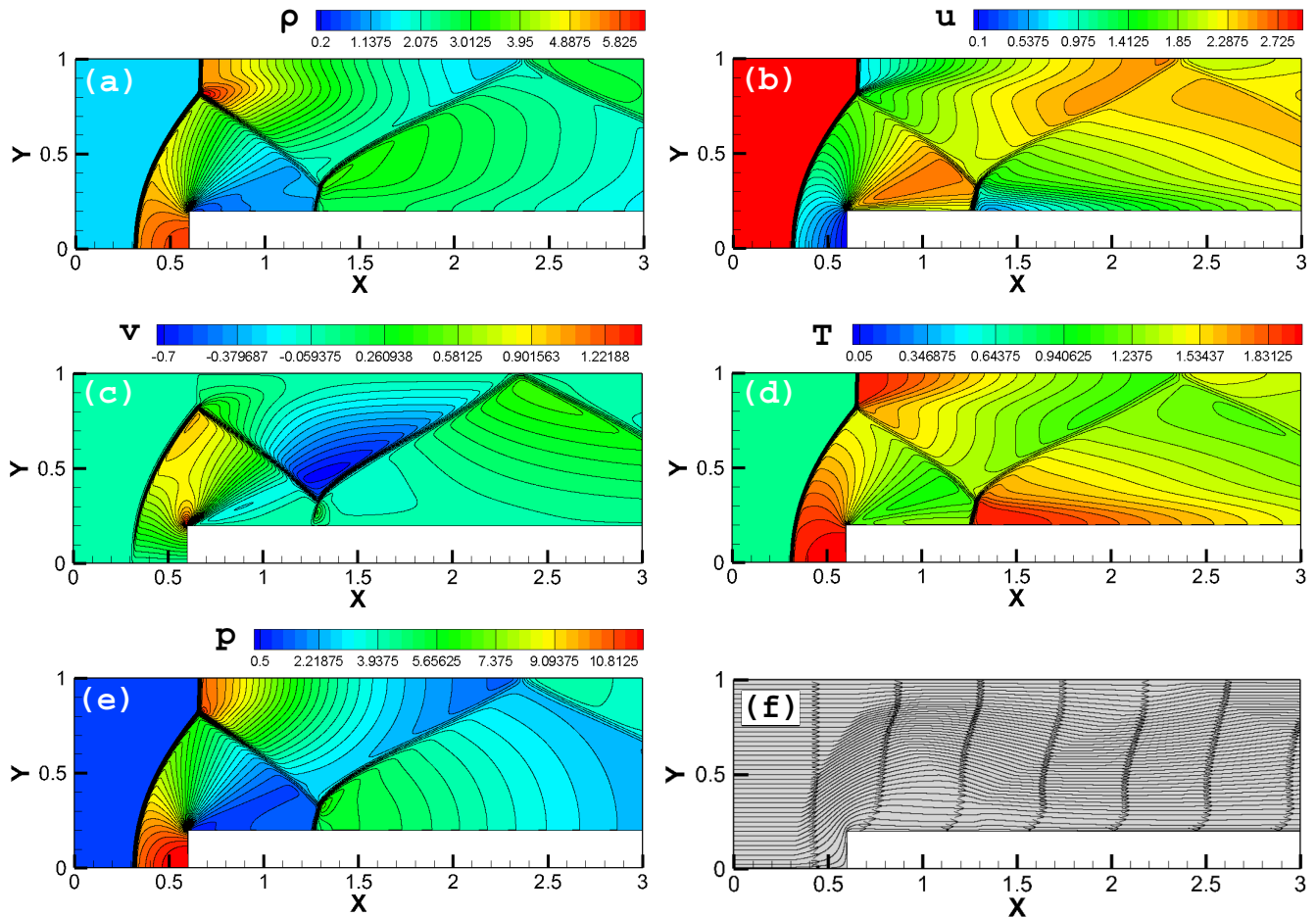


FIG. 28. Flow properties at steady-state for forward-facing step flow properties: $Ma = 3.0$, step height = 0.2, $\Delta x = 1.0/1000$, $\Delta t = 5 \times 10^{-5}$, and for $t = 4.0$, contour plots of (a) density, ρ , (b) x -direction velocity, u , (c) y -direction velocity, v , (d) temperature, T , (e) pressure, p , and (f) streamlines plot.

number 3 with step height 0.2 is simulated. Later, the effect of variation of the Mach number on the flow structure, shock standoff distance, the Mach stem location, and Mach stem height are examined. The description of the computational geometry and boundary conditions are given in Fig. 26. The wind tunnel considered is 1 unit in height and 3 units in length. The step is 0.20 units high and is located at 0.6 length units from the left-hand side end of the channel. The channel is assumed to have an infinite width in the direction orthogonal to the plane of the domain. At the left-hand side, the inlet (or the inflow) boundary condition is applied, and the right-hand side is kept at supersonic outlet. For the reported simulation studies, it is assumed that the channel is filled with an ideal gas (hence, the specific heat ratio is taken as $\gamma = 7/5$). Further, the computational domain is initialized with $\rho = 7/5$, $p = 1.0$, and velocities $u_1 = u = Ma$ and $u_2 = v = 0$. The temperature-field T is computed from the ρ and p using the nondimensional equation of state. Next, the evolution of the flow structures from initial ($t = 0.0$) to $t = 4.0$ is depicted in Fig. 27 for the flow over forward-facing step with a uniform inlet Mach number of 3 and a step height of 0.2. It is observed that a detached bow shock immediately develops ahead of the step, initially curving strongly toward the upper surface of

the step [see Fig. 27(a)]. The curvature of the bow shock decreases rapidly and strikes the upper boundary of the domain [see Figs. 27(b) and 27(c)]. The shock is reflected downward and strikes the upper surface of the step [see Figs. 27(d) and 27(e)]. The bow shock continues to flatten until the incident angle to the upper boundary of the domain is so large that a Mach reflection forms [see Fig. 27(f)]. The secondary Mach stem forms at the upper surface of the step [see Fig. 27(g)]. At the point of intersection of the incident, the normal and reflected shock waves gradually move upstream and away from the upper surface. Further, a slip surface separating regions of different velocities emanates horizontally from the intersecting shocks at the triple point system. A weak shock which is observed where the overexpanded flow around the step corner strikes the upper surface of the step [see Figs. 27(h)–27(j)].

The present simulation results for a step height of 0.2 are compared with the standard benchmark results from Woodward and Colella [60], Shu [76], Zhu and Shu [62], and Li *et al.* [77]. The physical properties such as density, x -direction velocity, y -direction velocity, temperature, and pressure with equally spaced contours, along with the streamline patterns at $t = 4.0$, are shown in Fig. 28. The contour plot of density is shown in Fig. 29 and is used to extract the features of

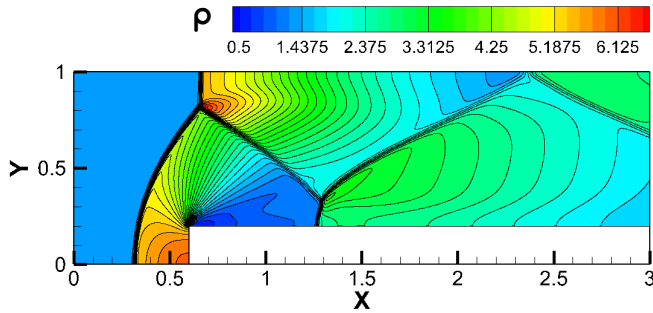


FIG. 29. Colour plot of density with 33 equally spaced contours for $Ma = 3$.

the flow structures. The shock standoff distance is a distance between the beginning of the step at the bottom surface and the bow shock generation point. The shock standoff distance as measured from the work of Woodward and Colella [60] is 0.302, from Shu [76] it is 0.28, from Zhu and Shu [62] it is 0.274, and from Li *et al.* [77] it is 0.29. The shock standoff distance is measured from the current simulation as 0.286. The secondary Mach stem location from the origin along the horizontal step as measured from the work of Li *et al.* [77] is 1.19, and from that of Zhu and Shu [62] is 1.264, whereas the secondary Mach stem is at a distance of 1.25 in the present work. The location of the triple-point system present in the flow because of the bow shock, reflected shock, and primary Mach stem is observed at (0.64, 0.83), whereas in Refs. [60,62,76,77] the locations are reported at $\approx(0.58, 0.75)$, $(0.62, 0.79)$, $(0.632, 0.81)$, and $(0.6, 0.77)$, respectively. Hence, it may be concluded that the present results are in a close agreement with the literature.

The effect of change in Mach number on the location of triple point and Mach stem along the step is easily recog-

nizable at time $t = 4.0$ as shown in Fig. 30. The primary triple point near the top wall is noticeable only in the case of inflow Mach number 3. It is observed that the secondary Mach stem and the secondary triple-point system are present in the considered cases except for the inflow Mach number of 2 [see Fig. 30(a)]. Further, the secondary Mach stem location is observed to be shifting toward the right-hand side of the computational domain along the step. The shock standoff distance is reduced with the increase in the inflow Mach number from 3 to 5 [Figs. 30(b)–30(d)]. Finally, the maximum and minimum values of the flow parameters keep on increasing with an increase in the flow Mach number. Further, the effect of change in the step height for the same boundary and initial conditions at $Ma = 3$ is detailed below. In order to carry out this work, the steps with 0.15, 0.2, and 0.25 unit height are considered at the equal distance from the inlet and outlet boundaries. The results (33 equally spaced contours of density in the computational domain) with a change in the step height for the same inlet boundary conditions with an uniform grid size of 1000×3000 at $t = 4.0$ are shown in Fig. 31. It is observed that in the case of step height of 0.25 units as shown in Fig. 31(c), the first triple-point system as well as first Mach stem are not realized as compared to those shown in Figs. 31(a) and 31(b). The similar flow structures are seen for the inflow Mach number of 2 [see Fig. 30(a)]. The shock standoff distance (from the forward step toward inlet) and secondary Mach stem location (along the step from origin) for the step heights of (0.15), (0.2), and (0.25), respectively are obtained as (0.216 and 1.838), (0.286 and 1.263), and (0.360, and absent). Further, from the above-measured distances it may be concluded that the shock standoff distance increases and the Mach stem location along the horizontal step

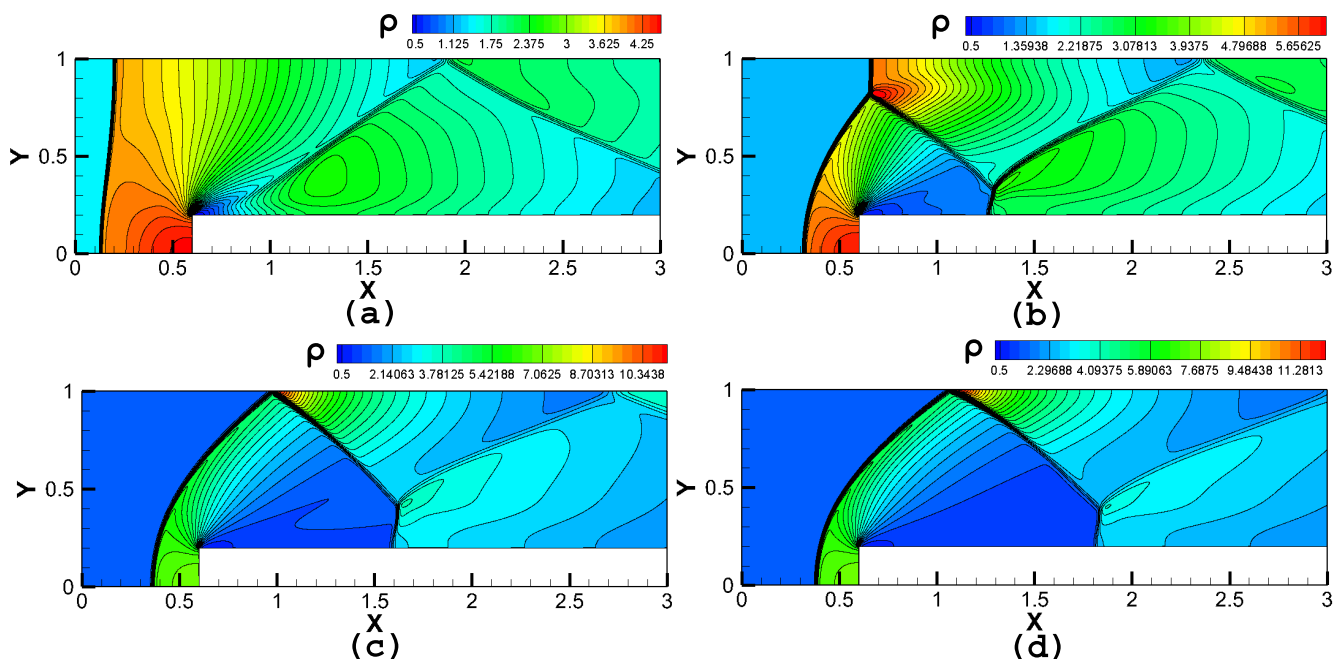


FIG. 30. Contour plots of density for various inflow Mach numbers, (a) $Ma = 2$, (b) $Ma = 3$, (c) $Ma = 4$, and (d) $Ma = 5$.

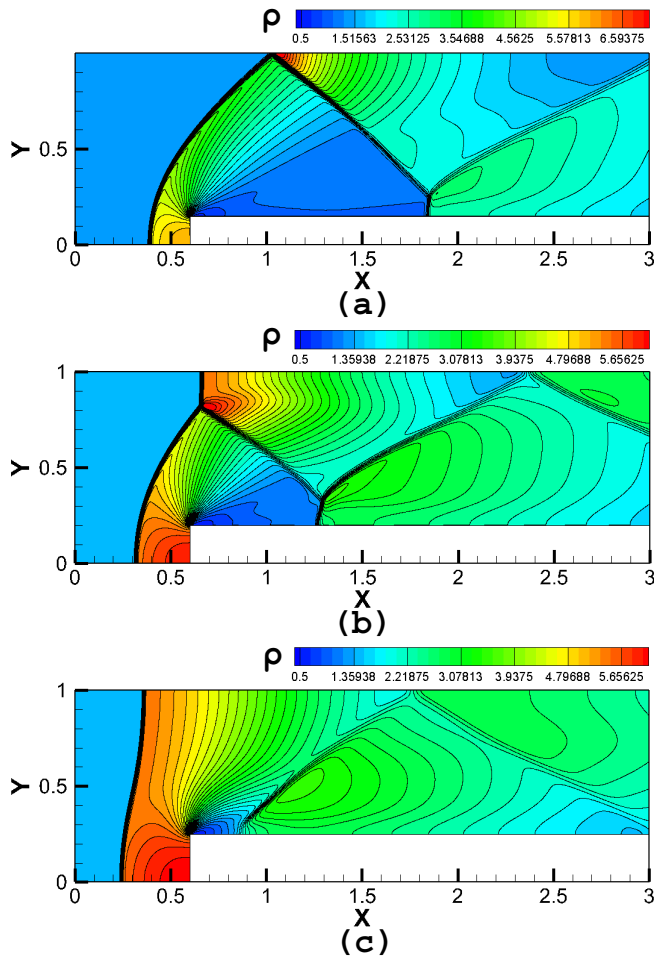


FIG. 31. Contour plots of density for various step heights: (a) 0.15; (b) 0.2; and (c) 0.25 for inlet Mach number of 3.

shifts toward the left side along the step with an increase in the step height.

Finally, the effect of change in specific heat ratios for a given Mach number is studied. In order to carry out this work, an inflow Mach number 3 is considered and the specific heat ratios were varied as $\gamma = 5/3$, $7/5$, and $9/7$. The results (33 equally spaced contours of density in the computational domain) for the inflow Mach number 3 with various specific heat ratios for the same inlet boundary conditions with a uniform grid size of 1000×3000 at $t = 4.0$ are shown in Fig. 32. The shock standoff distances (from the forward step toward inlet) and secondary Mach stem locations (along the step from origin) for the specific heat ratios of $\gamma = 5/3$, $\gamma = 7/5$, and $\gamma = 9/7$ are (0.527 and absent), (0.286 and 1.25), and (0.240 and 1.62), respectively. Further, from the above measured distances, it may be concluded that the shock standoff distance decreases and the Mach stem location along the horizontal step shifts toward the right side along the step with an increase in the specific-heat ratio. Also, it is important to note that the variations in the shock standoff distance and secondary Mach stem location follow similar trends as observed in the case of increase in Mach number variation. The secondary Mach stem is perpendicular to the step at the

bottom surface only in the case of $\gamma = 9/7$, whereas it is curved with $\gamma = 7/5$.

G. Numerical stability assessment

Here, the numerical stability assessment for the two-dimensional benchmark test cases are presented. The numerical stability analysis was studied in Refs. [78,79]. The additional parameters in the 2D, RK3 + WENO-based FD-LB formulation are introduced, namely, artificial viscosity and dissipation term. Hence, the objectives of the study are to investigate the numerical stability region and to generate guidelines for the values of the coefficients of the additional terms in the formulation. These studies help to identify the numerical stability when the additional terms are incorporated. In all the benchmark cases, initially the values of β_d and λ_{1-4} are varied in order to get the stable domain. Further, from the stable domain the effect of λ_{1-4} and β_d on keeping $\lambda_0 = v_1 dx$ and $\lambda_{5-8} = 0$ is studied in order to get the solution closer to the literature results for all the considered benchmarks. The corresponding results are presented below.

Regular shock reflection. In the case of regular shock reflection, it is observed that the $\lambda_{1-4}/v_1 dx$ gives stable solutions only for values greater or equal to 0.6. Moreover, the β_d values give a stable solution only if it is less than or equal to 0.5. The λ_{1-4} variation by keeping $\beta_d = 0$ is shown in Fig. 33(a). It implies that the lower value of λ_{1-4} is able to capture the shock accurately. Also, the variation of β_d values is studied by keeping λ_{1-4} constant as $v_1 dx$, and it suggests that the β_d value should be in between 0 to 0.5 as shown in Fig. 33(b). Here, the first shock is captured accurately by $\beta_d = 0.5$, whereas the second shock is captured accurately by $\beta_d = 0$. Hence, it is suggested that the value of λ_{1-4} should be small and the β_d value should be between 0 to 0.5.

Double Mach reflection. In the case of double Mach reflection, it is observed that the $\lambda_{1-4}/v_1 dx$ gives a stable solution except for 0, 0.1, and 1.0. Also, the β_d value gives a stable solution only if it is less than or equal to 0.4. The λ_{1-4} variation by keeping $\beta_d = 0$ is shown in Fig. 34(a). It indicates that the lower value of λ_{1-4} is able to capture the shock accurately. Also, the variation of β_d values is studied by keeping λ_{1-4} constant as $v_1 dx$, which implies that the β_d value should be close to 0 as shown in Fig. 34(b), since the lower value of β_d reduces the dispersion error which helps to produce a nonoscillatory solution. Hence, it is suggested that the value of λ_{1-4} should be small and the β_d value should be close to 0.

Forward-facing step. In the case of a forward-facing step, it is observed that the $\lambda_{1-4}/v_1 dx$ gives stable solutions for almost all the values. Moreover, the β_d values give a stable solution only if it is less than or equal to 0.5.

Further, λ_{1-4} is varied by keeping $\beta_d = 0$ as shown in Fig. 35(a). It indicates that the higher value of λ_{1-4} is able to capture the shock accurately and reduce the dissipation error. Also, Fig. 35(b) shows the variation of β_d values by keeping λ_{1-4} constant as $v_1 dx$, and it implies no significant changes in the curvature of the density profile. Hence, it is suggested that the value of λ_{1-4} should be high and the β_d value should be between 0 to 0.5.

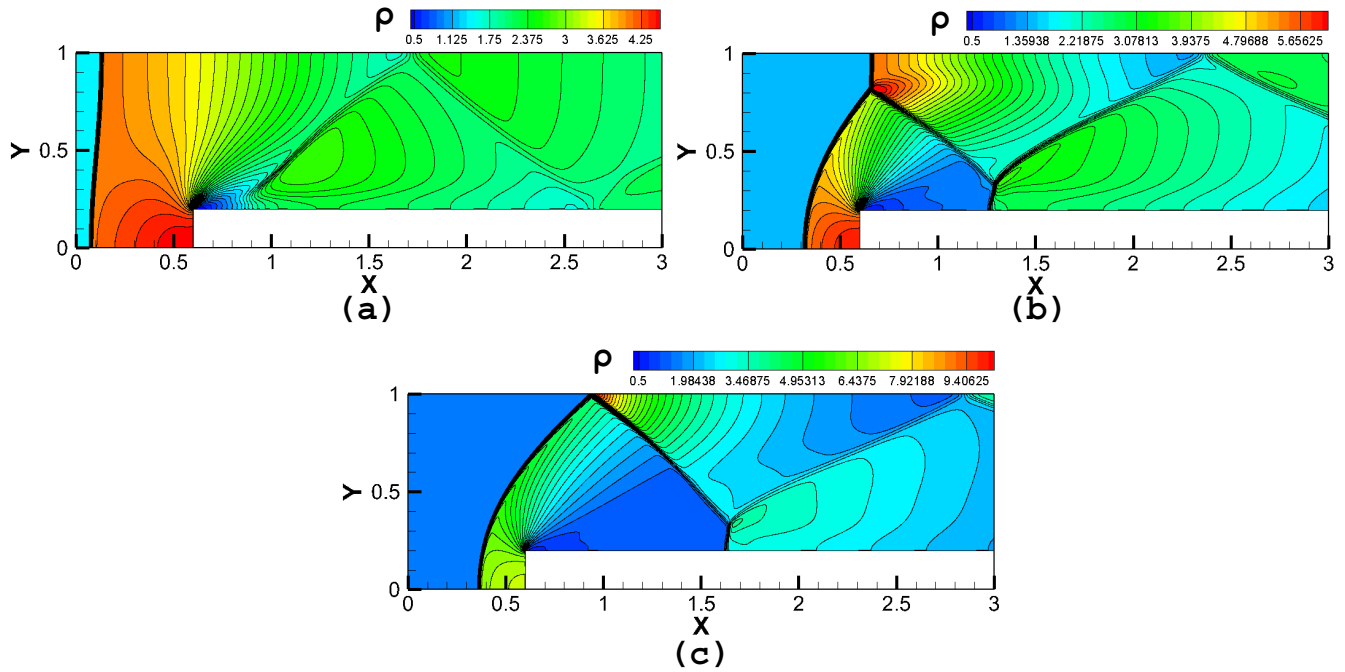


FIG. 32. Contour plots of density for various specific heat ratios for $Ma = 3$: (a) $\gamma = 5/3$, (b) $\gamma = 7/5$, and (c) $\gamma = 9/7$.

IV. CONCLUSION

In this paper, a numerical algorithm is detailed to simulate the inviscid compressible flow using the kinetic-theory-based lattice Boltzmann equation method. The LBE method composed of the discrete velocity model given by Kataoka and Tsutahara is utilized for solving the benchmark problems in one and two dimensions. In order to achieve higher order accuracy and to remove numerical oscillations, the fifth-order WENO scheme in space and third-order RK3 for time integra-

tion are incorporated in the finite-difference LBE framework. The dissipation and artificial viscosity terms may also be added in order to improve the stability of the scheme at a high Mach numbers and large density ratios. The article utilizes definition of various benchmark problems in the literature to verify and validate the proposed RK3 + WENO-based finite-difference LBE method. The 1D Riemann problems for various combinations of waves are detailed, which include the shock-shock waves with Mach numbers 1, 10, and 30, rarefaction-shock waves with density ratios 100 and 1000,

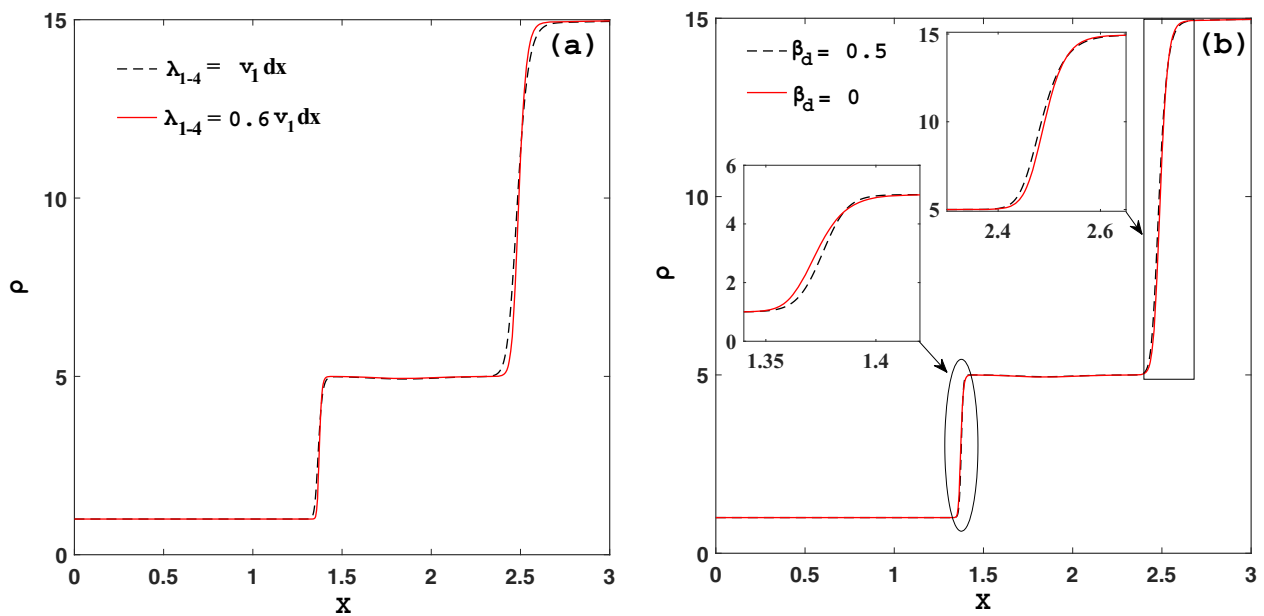


FIG. 33. Parametric variation for regular shock reflection for inflow $Ma = 10.0$ at $y = 0.2$: (a) λ_{1-4} variation with $\beta_d = 0$, $\lambda_0 = v_1 dx$ and (b) β_d variation with $\lambda_{1-4} = 0.6v_1 dx$, $\lambda_0 = v_1 dx$.

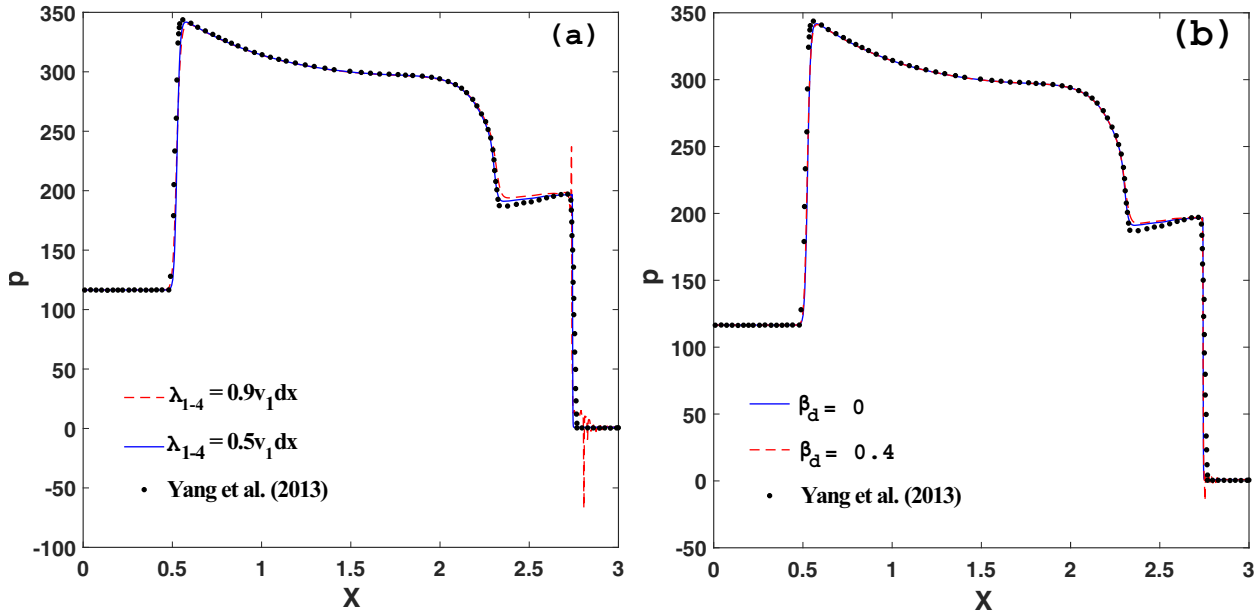


FIG. 34. Parametric variation for double Mach reflection for inflow $Ma = 10.0$ at $y = 0.3$: (a) λ_{1-4} variation with $\beta_d = 0$, $\lambda_0 = v_1 dx$ and (b) β_d variation with $\lambda_{1-4} = 0.5v_1 dx$, $\lambda_0 = v_1 dx$.

sudden contact shock discontinuity, and shock-rarefaction waves. The described parameters give good accuracy with very minimal deviation from the analytical solution. The isentropic vortex test conducted showed minimal reflections from the outflow boundary and negligible vortex distortion, proving accurate implementation of the outflow boundary condition and the presence of numerical viscosities in the acceptable range. The regular shock reflection results compare well with the analytical solution as well as with the line plot data from the literature. DMR with the change in Mach numbers and wedge angles are studied. It is observed that the shock

wave along the top wall covers more distance and the height of the primary Mach stem decreases as a result of an increase in the wedge angle of an DMR problem. The effect of change in wedge angle for same Mach number resulted in attached or detached shock pattern is also highlighted. In the case of the forward-facing step problem, the Mach stem at the top is visible after the Mach number reaches 2.75. The Mach stem location on the step shifts toward the right with an increase in inflow Mach number. Further, for the same inlet Mach number, the shock standoff distance is observed to be increased with the increase in the step height. The study

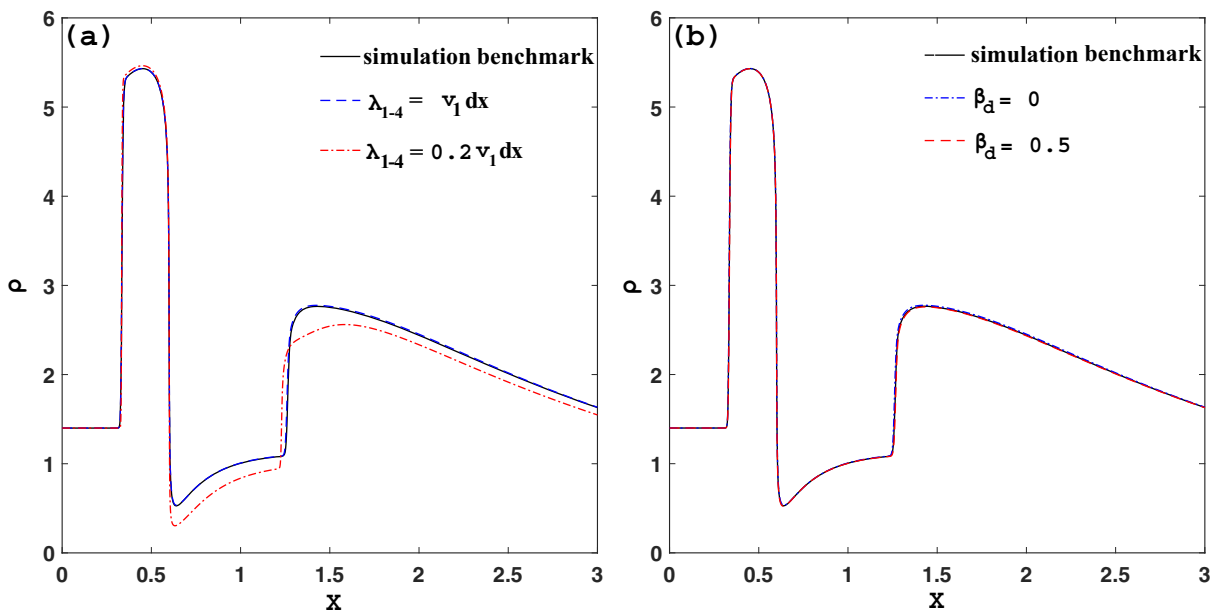


FIG. 35. Parametric variation for supersonic inviscid flow over a forward-facing step for inflow $Ma = 3.0$ at $y = 0.2$: (a) λ_{1-4} variation with $\beta_d = 0$, $\lambda_0 = v_1 dx$ and (b) β_d variation with $\lambda_{1-4} = v_1 dx$, $\lambda_0 = v_1 dx$.

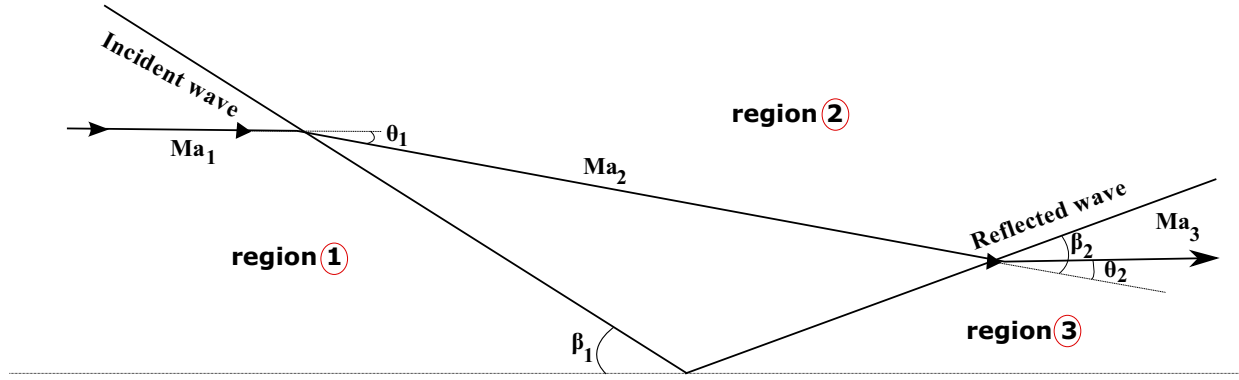


FIG. 36. Schematic of regular shock reflection problem depicting reflection.

of the variation in the specific heat ratio implies the shock standoff distance decreases and the Mach stem location along the horizontal step shifts toward the right side along the step. From the simulations of various benchmark problems, it is reported that the value of v_1 may be kept near to the Mach number, v_2 may be equal to two times the value of v_1 , and the value of η_0 may be taken as an average of v_1 and v_2 . Further, in the case of rarefaction-shock wave problem, the inflow Mach number is zero; however, for the consideration of high-density ratio, v_1 is kept as 3.0. The dissipation term is decided by taking into account the dissipation error and the stability criteria. The guidelines regarding the selection of the free parameters in the formulation are given. The studies regarding the local adaptation of the free parameters need to be carried out for subsonic and transonic flows. Further investigations regarding the secondary slip plane and Kelvin Helmholtz instability in the case of the DMR problem are needed.

The data that support the findings of this study are available from the corresponding author upon reasonable request.

ACKNOWLEDGMENTS

Authors thank the referees for the careful and insightful reviews of the manuscript. Authors also acknowledge the support of “AnantGanak: HPC facility at IIT Dharwad.” S.G.N. and D.V.P. acknowledge the support of ISRO-RESPOND and VSSC for Project “RESPOND-VSSC002.”

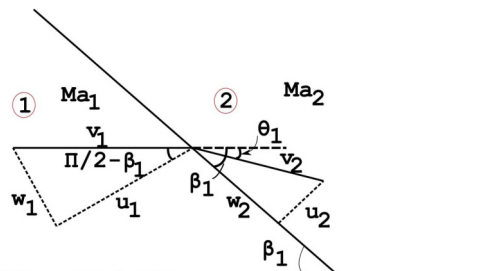


FIG. 37. Velocity components at regions ① and ②.

APPENDIX: ANALYTICAL SOLUTION OF REGULAR SHOCK REFLECTION

Consider Ma_1 , Ma_2 , and Ma_3 to be the Mach numbers in regions ①, ②, and ③, respectively, as shown in Fig. 36. θ_1 , θ_2 are the wedge angles for first and second waves and β_1 , β_2 are the shock wave angles. Figure 37 shows the velocity component schematic between regions ① and ②, whereas Fig. 38 shows the schematic for velocity resolution between regions ② and ③. Assuming properties in the region ① are known, properties at region ① can be calculated:

$$\frac{\rho_2}{\rho_1} = \frac{(\gamma + 1)Ma_1^2 \sin^2 \beta_1}{2 + (\gamma - 1)Ma_1^2 \sin^2 \beta_1}. \quad (A1)$$

Now, to calculate the wedge angle,

$$\tan \theta = \tan \beta_1 \frac{[Ma_1^2 \cos^2 \beta_1 - \cot^2 \beta_1]}{[1 + 1/2Ma_1^2(\gamma + \cos(2\beta_1))]} \quad (A2)$$

Mach number calculation in the region ② is

$$Ma_2^2 \sin^2(\beta_1 - \theta) = \frac{[\gamma + 1 + (\gamma - 1)(Ma_1^2 \sin^2 \beta_1 - 1)]}{[\gamma + 1 + 2\gamma(Ma_1^2 \sin^2 \beta_1 - 1)]}, \quad (A3)$$

and for calculating pressure,

$$\frac{p_2}{p_1} = \frac{[2\gamma Ma_1^2 \sin^2 \beta - (\gamma - 1)]}{(\gamma + 1)}. \quad (A4)$$

From Fig. 37, it is observed that $w_1 = v_1 \sin(\pi/2 - \beta_1)$ and $w_2 = v_2 \cos(\beta_1 - \theta_1)$. Since $w_1 = w_2$, the value of v_2 is calculated. Next, using v_2 , the values of u_2 and v_2 are then calculated. Moreover, the wedge angles are same in

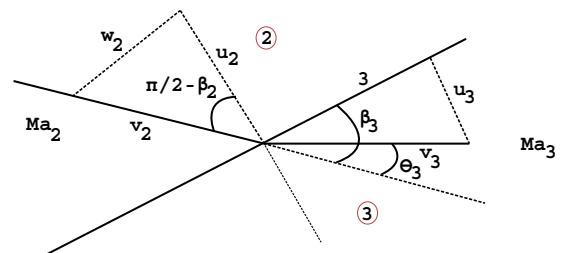


FIG. 38. Velocity components at regions ② and ③.

both the regions, and hence the value of β_2 is calculated from Eq. (A2). Finally, on similar lines, properties in the

region ③ can be calculated by using properties in the region ②.

-
- [1] T. Krüger, H. Kusumaatmaja, A. Kuzmin, O. Shardt, G. Silva, and E. M. Viggien, *The Lattice Boltzmann Method* (Springer, Berlin, 2017), Vol. 10, pp. 4–15
- [2] Z. Guo and C. Shu, *Lattice Boltzmann Method and Its Application in Engineering* (World Scientific, Singapore, 2013), Vol. 3.
- [3] C. K. Aidun and J. R. Clausen, *Annu. Rev. Fluid Mech.* **42**, 439 (2010).
- [4] M. Bouzidi, D. d’Humières, P. Lallemand, and L.-S. Luo, *J. Comput. Phys.* **172**, 704 (2001).
- [5] V. Zecevic, M. P. Kirkpatrick, and S. W. Armfield, *Comput. Fluids* **202**, 104492 (2020).
- [6] E. Yahia and K. N. Premnath, *Phys. Fluids* **33**, 057110 (2021).
- [7] L. Zhu, P. Wang, and Z. Guo, *J. Comput. Phys.* **333**, 227 (2017).
- [8] V. Sofonea, A. Lamura, G. Gonnella, and A. Cristea, *Phys. Rev. E* **70**, 046702 (2004).
- [9] A. Fakhari and T. Lee, *Phys. Rev. E* **89**, 033310 (2014).
- [10] D. V. Patil and K. Lakshmisha, *J. Comput. Phys.* **228**, 5262 (2009).
- [11] Z. Guo, K. Xu, and R. Wang, *Phys. Rev. E* **88**, 033305 (2013).
- [12] T. Lee and C.-L. Lin, *J. Comput. Phys.* **171**, 336 (2001).
- [13] Y. Li, E. J. LeBoeuf, and P. K. Basu, *Phys. Rev. E* **69**, 065701(R) (2004).
- [14] A. Bardow, I. V. Karlin, and A. A. Gusev, *EPL* **75**, 434 (2006).
- [15] A. Bardow, I. V. Karlin, and A. A. Gusev, *Phys. Rev. E* **77**, 025701(R) (2008).
- [16] J. D. Anderson, *Modern Compressible Flow: With Historical Perspective* (McGraw-Hill, New York, 1990), Vol. 12.
- [17] F. J. Alexander, H. Chen, S. Chen, and G. D. Doolen, *Phys. Rev. A* **46**, 1967 (1992).
- [18] Y. Qian, *J. Sci. Comput.* **8**, 231 (1993).
- [19] C. Sun, *Phys. Rev. E* **61**, 2645 (2000).
- [20] C. Sun and A. Hsu, *Comput. Fluids* **33**, 1363 (2004).
- [21] H. Yu and K. Zhao, *Phys. Rev. E* **61**, 3867 (2000).
- [22] T. Kataoka and M. Tsutahara, *Phys. Rev. E* **69**, 056702 (2004).
- [23] Y. Guangwu, C. Yaosong, and H. Shouxin, *Phys. Rev. E* **59**, 454 (1999).
- [24] A.-G. Xu, G.-C. Zhang, Y.-B. Gan, F. Chen, and X.-J. Yu, *Front. Phys.* **7**, 582 (2012).
- [25] F. Chen, A. Xu, G. Zhang, Y. Li, and S. Succi, *EPL* **90**, 54003 (2010).
- [26] X. Pan, A. Xu, G. Zhang, and S. Jiang, *Int. J. Mod. Phys. C* **18**, 1747 (2007).
- [27] Y. Gan, A. Xu, G. Zhang, X. Yu, and Y. Li, *Phys. A (Amsterdam, Neth.)* **387**, 1721 (2008).
- [28] T. Kataoka and M. Tsutahara, *Phys. Rev. E* **69**, 035701(R) (2004).
- [29] T. Kataoka and T. Hanada, *Int. J. Numer. Methods Fluids* **91**, 183 (2019).
- [30] T. Hanada and T. Kataoka, *Int. J. Numer. Methods Fluids* **93**, 2554 (2021).
- [31] M. Watari, *Phys. A (Amsterdam, Neth.)* **382**, 502 (2007).
- [32] G. Yan, J. Zhang, Y. Liu, and Y. Dong, *Int. J. Numer. Methods Fluids* **55**, 41 (2007).
- [33] M. Watari and M. Tsutahara, *Phys. Rev. E* **67**, 036306 (2003).
- [34] Q. Li, Y. L. He, Y. Wang, and W. Q. Tao, *Phys. Rev. E* **76**, 056705 (2007).
- [35] A. Jammalamadaka, G. M. Laskowski, Y. Li, J. Kopriva, P. Gopalakrishnan, R. Zhang, and H. Chen, in *AIAA Aviation 2020 Forum* (AIAA, Reston, VA, 2020), Paper No. AIAA 2020-3055.
- [36] J. Latt, C. Coreixas, J. Beny, and A. Parmigiani, *Philos. Trans. R. Soc. A* **378**, 20190559 (2020).
- [37] Y. Feng, P. Boivin, J. Jacob, and P. Sagaut, *J. Comput. Phys.* **394**, 82 (2019).
- [38] G. Farag, S. Zhao, T. Coratger, P. Boivin, G. Chiavassa, and P. Sagaut, *Phys. Fluids* **32**, 066106 (2020).
- [39] F. Renard, Y. Feng, J.-F. Boussuge, and P. Sagaut, *Comput. Fluids* **219**, 104867 (2021).
- [40] S. Guo, Y. Feng, and P. Sagaut, *Comput. Fluids* **219**, 104866 (2021).
- [41] S. Zhao, G. Farag, P. Boivin, and P. Sagaut, *Phys. Fluids* **32**, 126118 (2020).
- [42] P. Pavlo, G. Vahala, and L. Vahala, *Phys. Rev. Lett.* **80**, 3960 (1998).
- [43] P. Pavlo, G. Vahala, and L. Vahala, *J. Stat. Phys.* **107**, 499 (2002).
- [44] D. Wilde, A. Krämer, D. Reith, and H. Foysi, *Phys. Rev. E* **101**, 053306 (2020).
- [45] D. Wilde, A. Krämer, D. Reith, and H. Foysi, *Phys. Rev. E* **104**, 025301 (2021).
- [46] C.-W. Shu, *Advanced Numerical Approximation of Nonlinear Hyperbolic Equations* (Springer, Berlin, 1998), pp. 325–432.
- [47] X.-D. Liu, S. Osher, and T. Chan, *J. Comput. Phys.* **115**, 200 (1994).
- [48] G.-S. Jiang and C.-W. Shu, *J. Comput. Phys.* **126**, 202 (1996).
- [49] C.-W. Shu and S. Osher, *Upwind and High-Resolution Scheme* (Springer, Berlin, 1989), pp. 328–374.
- [50] C.-W. Shu, *SIAM Rev.* **51**, 82 (2009).
- [51] L. Yang, Y. Wang, Z. Chen, and C. Shu, *Lattice Boltzmann and Gas Kinetic Flux Solvers: Theory and Applications* (World Scientific, Singapore, 2020).
- [52] K. Hejranfar and E. Ezzatneshan, *Int. J. Numer. Methods Fluids* **75**, 713 (2014).
- [53] Y. Wang, Y. He, J. Huang, and Q. Li, *Int. J. Numer. Methods Fluids* **59**, 853 (2009).
- [54] D. S. Balsara and C.-W. Shu, *J. Comput. Phys.* **160**, 405 (2000).
- [55] O. Friedrich, *J. Comput. Phys.* **144**, 194 (1998).
- [56] J. Shi, C. Hu, and C.-W. Shu, *J. Comput. Phys.* **175**, 108 (2002).
- [57] P. Colella and H. M. Glaz, *J. Comput. Phys.* **59**, 264 (1985).
- [58] G. Ben-Dor, *Shock Wave Reflection Phenomena* (Springer, Berlin, 2007), Vol. 2.
- [59] R. Paciorri and A. Bonfiglioli, *J. Comput. Phys.* **230**, 3155 (2011).

- [60] P. Woodward and P. Colella, *J. Comput. Phys.* **54**, 115 (1984).
- [61] L. Yang, C. Shu, J. Wu, N. Zhao, and Z. Lu, *J. Comput. Phys.* **255**, 540 (2013).
- [62] J. Zhu and C.-W. Shu, *J. Comput. Phys.* **349**, 80 (2017).
- [63] X. He and L.-S. Luo, *Phys. Rev. E* **56**, 6811 (1997).
- [64] X. He and L.-S. Luo, *Phys. Rev. E* **55**, R6333(R) (1997).
- [65] S. Chapman and T. G. Cowling, *The Mathematical Theory of Non-uniform Gases: An Account of the Kinetic Theory of Viscosity, Thermal Conduction, and Diffusion in Gases* (Cambridge University Press, Cambridge, UK, 1990).
- [66] F. Renard, G. Wissocq, J.-F. Boussuge, and P. Sagaut, *J. Comput. Phys.* **446**, 110649 (2021).
- [67] P. Lallemand and L.-S. Luo, *Phys. Rev. E* **68**, 036706 (2003).
- [68] K. Qu, C. Shu, and Y. T. Chew, *Phys. Rev. E* **75**, 036706 (2007).
- [69] F. D. Lora-Clavijo, J. P. Cruz-Pérez, F. Siddhartha Guzmán, and J. A. González, *Revista Mex. Física E* **59**, 28 (2013).
- [70] M. Safdari Shadloo, *Numer. Heat Trans., Part A* **75**, 167 (2019).
- [71] Y. Feng, S. Guo, J. Jacob, and P. Sagaut, *Phys. Fluids* **31**, 017104 (2019).
- [72] L. Li, J. Zhu, and Y.-T. Zhang, *J. Comput. Phys.* **443**, 110516 (2021).
- [73] G. Ben-Dor and I. Glass, *J. Fluid Mech.* **92**, 459 (1979).
- [74] A. Rikanati, O. Sadot, G. Ben-Dor, D. Shvarts, T. Kuribayashi, and K. Takayama, *Phys. Rev. Lett.* **96**, 174503 (2006).
- [75] C. Zaza, Contribution to numerical methods for all Mach flow regimes and to fluid-porous coupling for the simulation of homogeneous two-phase flows in nuclear reactors, Ph.D. thesis, Aix Marseille Université, France, 2015.
- [76] C.-W. Shu, *High-Order Methods for Computational Physics* (Springer, Berlin, 1999), pp. 439–582.
- [77] Y. Li, X.-D. Niu, H.-Z. Yuan, A. Khan, and X. Li, *Acta Mech. Sin.* **34**, 995 (2018).
- [78] Y. Ning, K. N. Premnath, and D. V. Patil, *Int. J. Numer. Methods Fluids* **82**, 59 (2016).
- [79] L.-S. Luo, W. Liao, X. Chen, Y. Peng, W. Zhang, *Phys. Rev. E* **83**, 056710 (2011).